J. Fluid Mech. (2014), *vol.* 758, *pp.* 655–685. © Cambridge University Press 2014
doi:10.1017/jfm.2014.548

Self-sustained oscillations of shallow flow past sequential cavities

B. A. Tuna[1] **and D. Rockwell**[1,†]

[1]Department of Mechanical Engineering and Mechanics, Lehigh University, Bethlehem, PA 18015, USA

(Received 9 March 2014; revised 10 August 2014; accepted 16 September 2014;
first published online 10 October 2014)

Shallow flow past successive cavities is characterized by means of high-image-density particle image velocimetry (PIV). Highly coherent, self-sustained oscillations arise due to coupling between the inherent instability of the separated shear layer along the opening of each sequential cavity; and a gravity standing wave mode within each cavity. The globally coupled nature of the flow structure is evident through dominance of the same spectral component in the undulating vorticity layers along each of the successive cavities and the wall pressure fluctuations within the cavities. Unlike coupled phenomena associated with flow past a single cavity, optimal coupling for successive cavities requires a defined phase shift between the gravity standing wave patterns in adjacent cavities and, furthermore, an overall phase shift of the undulating shear layer along the cavity openings. The magnitudes of these phase shifts depend on the mode of the gravity standing wave in each cavity, i.e. longitudinal or transverse mode, which is respectively aligned with or normal to the main stream. Such phase shifts result in corresponding displacements of patterns of phase-referenced vorticity concentrations along the cavity openings and changes in the timing of impingement of these concentrations upon the downstream corners of successive cavities. All of the foregoing aspects are related to the unsteady recirculation flow within the cavity, the time-dependent streamline topology, and concentrations of Reynolds stress along the cavity opening.

Key words: shallow water flows, surface gravity waves, vortex interactions

1. Introduction

Turbulent shallow flows in estuaries, lakes, coastal areas and rivers can exhibit instabilities in the horizontal plane. Such instabilities have length scales that are much larger than the water depth. A feature of shallow flows is the presence of a shear-supporting bottom surface (bed) and a free surface. Both boundaries suppress vertical motions and restrict the length scale of the three-dimensional turbulence L_T, which is of an order less than the water depth h_w, i.e. $L_T \leqslant h_w$. As described by Jirka & Uijttewaal (2004), the characteristic diameter D of two-dimensional turbulent vortical structures in the horizontal plane is much larger than the water depth, that is, $D \gg h_w$. Uijttewaal & Tukker (1998) state that the no-slip condition at the bed

† Email address for correspondence: dor0@lehigh.edu

https://doi.org/10.1017/jfm.2014.548 Published online by Cambridge University Press

leads to the production of turbulence with three-dimensional characteristics, while the slip condition at the free surface enhances two-dimensional effects. Stansby (2003) describes the consequence of three-dimensionality on bed shear. In the vertical boundary layer, vertical and horizontal turbulence structures interact, the associated vertical mixing promotes uniformity of the velocity distribution in the vertical direction and, at the bed, where the velocity is zero, the velocity gradient and thereby the bed shear are enhanced.

In recent decades, a number of researchers have addressed the flow patterns in rivers in the presence of groyne fields, dead zones or embayments, which have important consequences for sediment transport, dispersion of pollutants, erosion and maintenance of aquatic life. Shallow river flow past two consecutive groynes that form a cavity is a representative example of a shallow mixing layer having a finite streamwise extent. In the field, a succession of groynes typically occurs, thereby forming a succession of cavities. The primary aim of this investigation is to determine the flow physics and exchange processes for successive cavities.

1.1. *Instability of a shallow mixing layer*

Laboratory investigations, as well as numerical simulations and analyses, have resulted in substantial advances in our understanding of shallow mixing layers. Jirka (2001) defined various generation mechanisms for two-dimensional turbulent coherent structures in shallow flows, which play an important role in the mass and momentum exchange processes between the main river flow and the groyne field. Uijttewaal (2011) assessed several mechanisms that govern the exchange of mass and momentum in shallow mixing layers. According to the experiments of Bian *et al.* (2011), large-scale vortices form from roll-up of the separated turbulent layer, and these vortices interact with the recirculating flow within the cavity. Different approaches to modelling the growth of shallow mixing layers were developed by Babarutsi & Chu (1993, 1998), Booij & Tukker (2001), van Prooijen & Uijttewaal (2002) and Biron, Ramamurthy & Han (2004). Tukker & Booij (1996), Uijttewaal & Booij (2000) and Uijttewaal, Lehmann & Mazijk (2001) analysed the effect of water depth on shallow mixing layers, and found that it influenced the development of large-scale coherent structures. An established feature of all of these models and analyses is reduction of the rate of growth of a mixing layer by bottom friction.

Alavian & Chu (1985) addressed the stability of turbulent exchange flow in a shallow compound channel and numerically determined neutral stability curves. Chu & Babarutsi (1988) experimentally studied the effect of bed friction on a shallow mixing layer. In addition, they carried out a corresponding instability analysis. A bed-friction number S was defined as $S = \overline{c}_f \delta \overline{U}/h_w \Delta U$, where $\overline{c}_f$ is the bed-friction coefficient, δ is the width of the transverse shear flow, $\overline{U}$ is the average velocity across the shear layer, ΔU is the corresponding velocity difference across the shear layer and h_w is the water depth. They found the critical value to be $S_{cr} = 0.09$; below this threshold, bed friction could not stabilize the flow. Babarutsi, Ganoulis & Chu (1989) and Babarutsi & Chu (1991) experimentally investigated mixing in shallow recirculating flows, and showed a reduction in transverse mixing due to bed friction. Chu, Wu & Khayat (1991) characterized channel flow with floodplains, which created a shallow mixing layer due to the different values of bottom friction in the transverse direction; for this configuration, the critical value was $S_{cr} = 0.12$.

Socolofsky & Jirka (2004) employed the rigid-lid assumption in their linear stability analysis to determine critical values of the bed-friction parameter. They found that

https://doi.org/10.1017/jfm.2014.548 Published online by Cambridge University Press

the onset of instability was enhanced due to the large velocity gradient across the mixing layer, and these instabilities resulted in large-scale coherent structures, which had a remarkable influence on the exchange processes. The accuracy of the rigid-lid assumption for stability analyses of shallow flows was analysed by Kolyshkin & Ghidaoui (2003) and Nazarovs (2005). The error in using the rigid-lid assumption was small for small values of Froude number $Fr = U/(gh_w)^{1/2}$, and it became larger when $Fr > 1$. Kolyshkin & Ghidaoui (2002) carried out an assessment of the effect of Froude number on the stability of shallow mixing layers in compound and composite channels. They reported that one can employ the rigid-lid assumption within 10 % error in the regime $0 < Fr < 0.7$ when determining the critical values of the stability parameter S, i.e. the bed-friction number.

1.2. *Shallow flow past a single cavity*

In recent years, a number of researchers, such as Engelhardt *et al.* (2004), Ribi, Boillat & Schleiss (2010) and Fujihara, Sakurai & Okamoto (2011), have analysed the ecological value of irrigation channels and rivers with groyne fields or embayments. Experimental and numerical studies have been conducted to reveal the flow physics within these configurations. Weitbrecht & Jirka (2001) and Kurzke, Weitbrecht & Jirka (2002) experimentally investigated the effects of a groyne field on the flow patterns in rivers and the associated exchange processes. According to their results, large-scale coherent structures played important roles in the momentum and mass exchange processes. This phenomenon was also indicated in the numerical study of McCoy, Constantinescu & Weber (2007). Mizumura & Yamasaka (2002) and Riviere *et al.* (2010) studied the recirculation flow patterns in a groyne field, and showed that the depth of the shallow water layer, main stream velocity and the aspect ratio of the groyne field affected the flow patterns. Uijttewaal (2005) and Kang, Yeo & Kim (2012) revealed the effects of geometry of the groyne field on the flow patterns and exchange processes. More recently, Sanjou & Nezu (2013) conducted an experimental study to examine the change in the flow structure inside the groyne field by varying the bed slope. In their experiments, the turbulence characteristics of the shear layer at the interface between the groyne field and the main stream, as well as the recirculating flow pattern inside the groyne field, showed different features at different values of bed slope. Sanjou & Nezu (2013) further noted that the mass exchange velocity between the main stream and the groyne field increased in accord with large magnitudes of Reynolds stress in the separated shear layer.

The enhancement of turbulent Reynolds stresses in the shear layer was related to the onset of a longitudinal gravity standing wave within the cavity by Wolfinger, Ozen & Rockwell (2012) and Tuna, Tinar & Rockwell (2013). Field experiments by Kimura & Hosoda (1997). Ikeda, Yoshike & Sugimoto (1999), Nezu & Onitsuka (2002), Ohmoto, Hirakawa & Watanabe (2005) and Kadotani *et al.* (2008) showed water-surface oscillation inside a cavity-like geometry, i.e. a groyne field, dead zone or embayment. It was suggested that such fluctuations may have been due to coupling between the inherent instability of the separated shear layer along the cavity opening and the gravity standing wave mode within the cavity.

1.3. *Shallow flow past a series of cavities*

The foregoing investigations of flow past a single groyne field, an embayment or a cavity have provided valuable insight into the flow structure and associated exchange processes. A number of investigations have revealed the flow patterns past a series

https://doi.org/10.1017/jfm.2014.548 Published online by Cambridge University Press

of groynes. Sukhodolov, Uijttewaal & Engelhardt (2002), Sukhodolov *et al.* (2004) conducted field work on the Elbe River in Germany in order to establish velocity and turbulence patterns inside groyne fields. Sukhodolov *et al.* (2002, 2004) reported that the patterns of recirculation flow did not significantly change with the downstream location. A computational study by Ercan & Younis (2009) on the Sacramento River, which simulated bank erosion in the presence of a series of cavities, showed important effects of the flow patterns.

In addition to field work, laboratory investigations and analyses have been carried out both numerically and experimentally. Wallast, Uijttewaal & van Mazijk (1999) and Uijttewaal *et al.* (2001) visualized the flow past a series of groyne fields and used dye to give insight into the mass exchange process. Both studies indicated that the structure of the shear layer between the groyne fields and the main stream varied with downstream position. Wallast *et al.* (1999) observed a decrease in the mass exchange coefficient with downstream location within the multiple groyne fields, while Uijttewaal *et al.* (2001) noted that each groyne field exhibited essentially similar mass exchange characteristics regardless of the downstream position. Furthermore, Muto, Imamoto & Ishigaki (2000) conducted an experimental study with three successive square embayments, and their results demonstrated differences in strength of the recirculating flow inside each groyne field. Ohmoto, Hirakawa & Watanabe (2009) examined the effects of angle of the groynes on the flow structure in the presence of two successive groyne fields; oscillation of the free surface inside the groyne field was detected. Moreover, Yaeger & Duan (2010) quantitatively analysed the effects of orientation of dikes for a series of three dikes, i.e. two successive cavities, by using a micro-acoustic Doppler velocimetry technique. A larger magnitude of Reynolds stress along the cavity opening was attained in the presence of angled dikes. More recently, the flow in the vicinity of the groynes was investigated by Yossef & de Vriend (2011) in order to assess sediment transport between the main stream and consecutive groyne fields. Yossef & de Vriend (2011) concluded that the sediment transport process was dependent on large-scale coherent structures, and the structure of the mixing layer along the opening of the groyne field changed with the downstream location. In the computational studies of McCoy, Constantinescu & Weber (2008) and Constantinescu, Sukhodolov & McCoy (2009), the mass exchange process and the flow characteristics along a series of groyne fields were analysed. Both studies used the rigid-lid assumption, where the free surface of the water was modelled as a rigid, horizontal boundary with slip. Constantinescu *et al.* (2009) found that the value of the mass exchange coefficient decreased with downstream location within the groyne field; this phenomenon was previously observed by Wallast *et al.* (1999). McCoy *et al.* (2008) indicate that a jet-like flow, parallel to the downstream groyne of each groyne field, was responsible for the momentum and the mass exchange processes between the main stream and the groyne fields.

The foregoing investigations have yielded substantial advances in our understanding of shallow flow past sequential cavities. A major unresolved issue is, however, the effect of gravity standing waves within the cavities, their coupling with vortex initiation and development along the openings of the cavities, and the manner in which this coupling influences the time-dependent and time-averaged flow patterns. More specifically, the orientation of, and phase shift between, gravity standing waves in successive cavities, as well as the phase variations in the separated shear layer along the openings of these cavities, are expected to exert a major influence. In turn, these effects will influence the mass exchange between the cavities and the mainstream. The present investigation addresses these characteristics using a

https://doi.org/10.1017/jfm.2014.548 Published online by Cambridge University Press

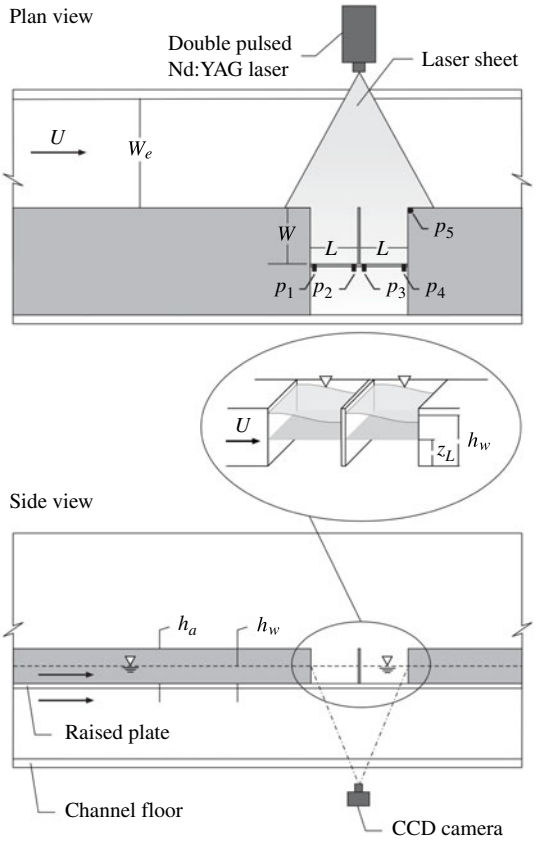


FIGURE 1. Schematic of experimental facility.

technique of high-image-density particle image velocimetry (PIV) combined with unsteady pressure measurements, in order to provide global representations of velocity, vorticity and turbulence statistics.

2. Experimental system and techniques

Experiments were conducted in a recirculating free-surface water channel. Upstream of the test section, the flow passes through a flow conditioning unit, which includes honeycombs and screens to yield a turbulence intensity of 0.2 %. The main test section has a length of 4877 mm, a width of 927 mm and an adjustable depth of 610 mm. The goal of this investigation was to determine the flow structure along and within two successive cavities. A test-section insert was designed and constructed to control the water depth, the dimensions of cavities and the flow velocity. Detailed schematics of the experimental system are given in figure 1, which indicates two perspectives of the experimental facility. Full details of the experimental system are given in the work of Tuna *et al.* (2013), which focused on shallow flow past a single cavity.

For all experiments described herein, each cavity had an aspect ratio $L/W = 0.66$, having a length of $L = 152$ mm and a width of $W = 228$ mm. The nominal water level was adjusted to a value of $h_w = 38$ mm, and the width of the channel was $W_e = 470$ mm as shown in figure 1. The streamwise length of the shallow water

https://doi.org/10.1017/jfm.2014.548 Published online by Cambridge University Press

layer, i.e. the distance from the leading edge of the horizontal raised (Plexiglas) plate to the leading (upstream) corner of the cavity was $L_i = 1908$ mm. Thus, the ratio of the inflow length L_i to water depth h_w was $L_i/h_w = 50.1$, which corresponds to the criterion of Uijttewaal *et al.* (2001) for a fully developed turbulent flow. This fully developed condition is central to extending the findings to different scales. When this condition is maintained, vortical structures in shallow flows, as well as the instabilities leading to their formation, which have been observed in a wide range of field experiments, can be effectively modelled in laboratory experiments, as described in the works of Jirka (2001), Jirka & Uijttewaal (2004) and Socolofsky & Jirka (2004).

The onset of hydrodynamic and gravitational instabilities in free-surface (shear-free) shallow water flows was identified by Ghidaoui & Kolyshkin (1999), and their criterion for these instabilities is determined by the Froude number $U/(gh_w)^{1/2}$. The flow is free of gravitational instabilities below the critical Froude number, i.e. $Fr < 1$. In the present configuration, the corresponding values of Froude number based on the water depth $h_w = 38$ mm and the depth-averaged inflow velocities $U = 273$ mm s^{-1} and 475 mm s^{-1} corresponding to resonant response were respectively $Fr = 0.45$ and $Fr = 0.71$. These values of Froude number are in the subcritical range and gravitational instabilities do not have a significant role. Furthermore, values of Reynolds number Re based on the width W of the inflow channel were $Re_W = 1.28 \times 10^5$ and 2.03×10^5, and based on the water depth h_w, $Re_{h_w} = 1.04 \times 10^4$ and $Re_{h_w} = 1.64 \times 10^4$.

Chu & Babarutsi (1988) experimentally investigated the transverse development of the shallow mixing layer in an open channel flow, and determined the stability of shallow mixing layers in terms of a dimensionless stability parameter $S = \overline{c}_f \delta \overline{U}/h_w \Delta U$. The bed friction coefficient $\overline{c}_f$ was calculated with their correlation $1/\sqrt{\overline{c}_f} = -4\log(1.25/Re\sqrt{\overline{c}_f})$, and the shear layer thickness δ was determined via the velocity field data from PIV. The values of the stability parameter S determined herein are $S = 0.007$ for the transverse mode of the gravity standing wave and $S = 0.004$ for the longitudinal mode (streamwise-oriented) of the gravity standing wave; these values are of the same order as determined in the experiments of Chu & Babarutsi (1988). Furthermore, these values of S are below the critical stability parameter range $S_{cr} = 0.01$–0.1 determined by Kolyshkin & Ghidaoui (2002) who concluded that bed friction does not stabilize the flow below S_{cr}, and instabilities occur due to the destabilizing effect of the velocity difference ΔU across the shear layer.

In the present investigation, only gravity standing wave modes oriented parallel and orthogonal to the streamwise direction are excited. These modes are associated respectively with the cavity length L and depth W, that is, each mode is governed by a single length scale. The two-dimensionality of each of these modes was verified with high-resolution video measurements of the free-surface deflection. The resonant frequency of the experimentally observed gravity standing wave in each of the cavities shown in figure 1 is calculated as follows. The eigenfrequency f_n of the fundamental eigenmode for a one-dimensional gravity standing wave pattern oriented in the transverse direction, corresponding to open and closed end conditions, is given by Naudascher & Rockwell (1994) as $f_n = \sqrt{gh_w}/4W$, in which W is the cavity width, h_w is the water depth, g is the gravitational acceleration and f_n is the frequency of the oscillation. The predicted frequency of this mode is calculated as $f_n = 0.66$ Hz; it compares well with the experimentally determined value of $f_n = 0.63$ Hz. On the other hand, the eigenfrequency of the fundamental eigenmode for a one-dimensional gravity standing wave oriented in the longitudinal direction, corresponding to a closed–closed end conditions is $f_n = \sqrt{gh_w}/2L$, in which L is the cavity length. The theoretically calculated value is $f_n = 2.00$ Hz, which compares well with the experimental frequency

https://doi.org/10.1017/jfm.2014.548 Published online by Cambridge University Press

of $f_n = 1.96$ Hz. These self-excited transverse and longitudinal modes of the gravity standing waves within each of the cavities corresponded to amplitudes h_d of the free-surface deflection that were an order of magnitude smaller than the nominal water depth h_w, i.e. $h_d/h_w = 0.049$ and $h_d/h_w = 0.094$.

A technique of high-image-density PIV led to quantitative determination of the flow patterns along and within the cavities. The major components of this system are indicated in figure 1. The laser sheet of 1 mm thickness was positioned at mid-depth, that is, midway between the nominal elevation h_w of the free-surface and the bed ($z_L/h_w = 0.5$). This sheet was generated by a dual pulsed Nd:Yag laser system having a maximum output of 90 mJ/pulse. The flow was seeded with 12 μm metallic-coated hollow plastic spheres at a sufficiently high density such that the interrogation window of 32 pixel × 32 pixel typically contained approximately 15–20 particles. A digital charge-coupled device (CCD) sensor camera with an array of 1600 pixel × 1192 pixel was placed below the water channel orthogonal to the horizontal plane of the laser sheet, as shown in the side view of figure 1. The aforementioned double-pulsed laser and camera were triggered by a synchronizer. The framing rate of the camera was 30 f.p.s. which gave 15 sets of image pairs per second. The effective magnification of the camera provided a resolution of 4.2 pixel mm^{-1} in the plane of the laser sheet. The patterns of particle images were processed using a frame-to-frame cross-correlation technique, and an overlap of 50 % was used in accord with the Nyquist criterion. This technique resulted in 7227 vectors with an effective grid size of 3.7 mm. The estimated uncertainties of the streamwise and transverse velocity measurements, which were calculated using the scheme of Adrian & Westerweel (2010), were 2 % of the depth-averaged free-stream velocity U.

PCB piezoelectric pressure transducers (model number 106B50) were employed for unsteady pressure measurements at five different locations. The pressure transducer p_5 was located at the impingement corner of the trailing (downstream) cavity at an elevation of $h_p = 13$ mm, as indicated in figure 1, in order to determine the frequency and amplitude of the shear layer oscillations. The pressure transducers $p_{1–4}$ were located at the back side of the cavity at a location 5 mm from the edges at an elevation of $h_p = 13$ mm from the bed (bottom surface). They were employed to determine the phase shifts between pressure fluctuations in adjacent cavities and the free-surface elevations. The correlation between millimetres of free-surface deflection and voltage output of these transducers was 10.85 mm V^{-1}. The unsteady pressure p_4 at the back wall of the cavity, as indicated in the plan view in figure 1, served as a reference signal in the phase-referencing process. These transducers had a nominal sensitivity of 72.5 mV kPa^{-1}. To adjust the gain of the transducer, the pressure transducers were connected to a PCB Piezotronics Sensor Signal Conditioner (model number 481A), which also employed a low-pass analogue filter at a cutoff frequency of 10 Hz. The conditioned analog pressure signals were converted to digital format by a PCI-MIO-16E-4 multichannel data acquisition board from National Instruments. For the pressure analyses, the sampling rate was set to 20 samples per second, corresponding to a Nyquist frequency of 10 Hz, which was well above the typical maximum frequency of interest in the present study. Sampling was conducted over a time span of 102.4 s, corresponding to a total of 2048 samples. Ten of these time records were acquired for each inflow velocity. Furthermore, in order to allow phase referencing during the PIV experiments, a sampling rate of 20 kS s^{-1} was selected.

The amplitude of the free-surface fluctuation was determined by using a high-definition camera focused on the junction between the free surface and the vertical wall of the cavity; simultaneously, unsteady pressure measurements were acquired. The

https://doi.org/10.1017/jfm.2014.548 Published online by Cambridge University Press

aforementioned correlation was employed to convert the transducer output in volts to the free-surface deflection in millimetres at the antinode of the gravity standing wave located along the wall of the cavity. This was accomplished by analysing instantaneous images from the high-definition camera and unsteady pressure measurements. The patterns plotted in figure 9 were determined by combining the amplitude values from the pressure transducers p_{1-4} and standing wave theory.

The unsteady pressure in the cavity and the Q-Switch synch out signal of the laser were used to determine the phase of the flow structure in the oscillation cycle. The size of the phase window at a nominal value of phase was 10°, where the complete oscillation cycle corresponded to 360°. For each set of PIV experiments, 200 sets of images were recorded simultaneously with the pressure signal. A total of 15 sets of experiments were conducted, and 3000 sets of images were recorded. The time-averaged flow structure was evaluated by averaging 3000 instantaneous velocity fields. The phase-referencing technique involved a minimum of 60 velocity fields per phase, which were used to determine the phase-averaged velocity, vorticity and streamline topology.

3. Concept of coupling between shear layer and gravity standing wave

A fluid-resonant cavity oscillation involves coupling of the inherent instability of the unstable separated shear layer along the cavity opening with one or more modes of a gravity standing wave within the cavity (Rockwell & Naudascher 1978). This coupling occurs when the frequency of a highly amplified disturbance in the separated shear layer coincides with an eigenfrequency of the gravity standing wave within the cavity. The reader is referred to Wolfinger *et al.* (2012) for a review of lock-on phenomena related to the present concept. Figure 2 illustrates the features of shallow flow past a single cavity (defined in the schematic in the inset) with and without a gravity standing wave, which is oriented in the streamwise direction. Figure 2(*a*) shows the time-dependent pressure fluctuations within the cavity, and figure 2(*b*,*c*) represent the spectra of these pressure fluctuations. Existence of the gravity standing wave, designated by the solid line in figure 2(*a*), is associated with large-amplitude pressure fluctuations within the cavity, and results in a well-defined spectral peak in figure 2(*c*). On the other hand, the spectral peak without the gravity standing wave is barely detectable, as shown in figure 2(*b*).

Corresponding patterns of instantaneous vorticity are shown in figure 2(*d*,*e*). In figure 2(*d*), there is lack of a coherent vortical structure in absence of a gravity standing wave; different scales associated with background turbulence are present. On the other hand, in figure 2(*e*), a large-scale, highly coherent vortex in the shear layer is associated with the gravity standing wave. This large-scale vortex is a result of disturbance amplification in the streamwise direction, starting from a low-amplitude transverse undulation of the separated shear layer at a location immediately downstream of the separation corner to progressively larger amplitude and eventually rolls up into the coherent vortex. Comparison of the patterns of vorticity in figure 2(*d*,*e*) is remarkably similar to the comparison given by Fiedler & Mensing (1985). In their experiment, localized (acoustic) excitation was applied at the separation corner, that is, the origin of the separated shear layer, and the perturbed shear layer evolved to the same type of large-scale vortical structure indicated in figure 2(*e*). The most receptive region of the separated shear layer is at the separation corner, so irrespective of whether the excitation is applied in a localized manner at the corner or over the entire extent of the shear layer, the conversion to vorticity

https://doi.org/10.1017/jfm.2014.548 Published online by Cambridge University Press

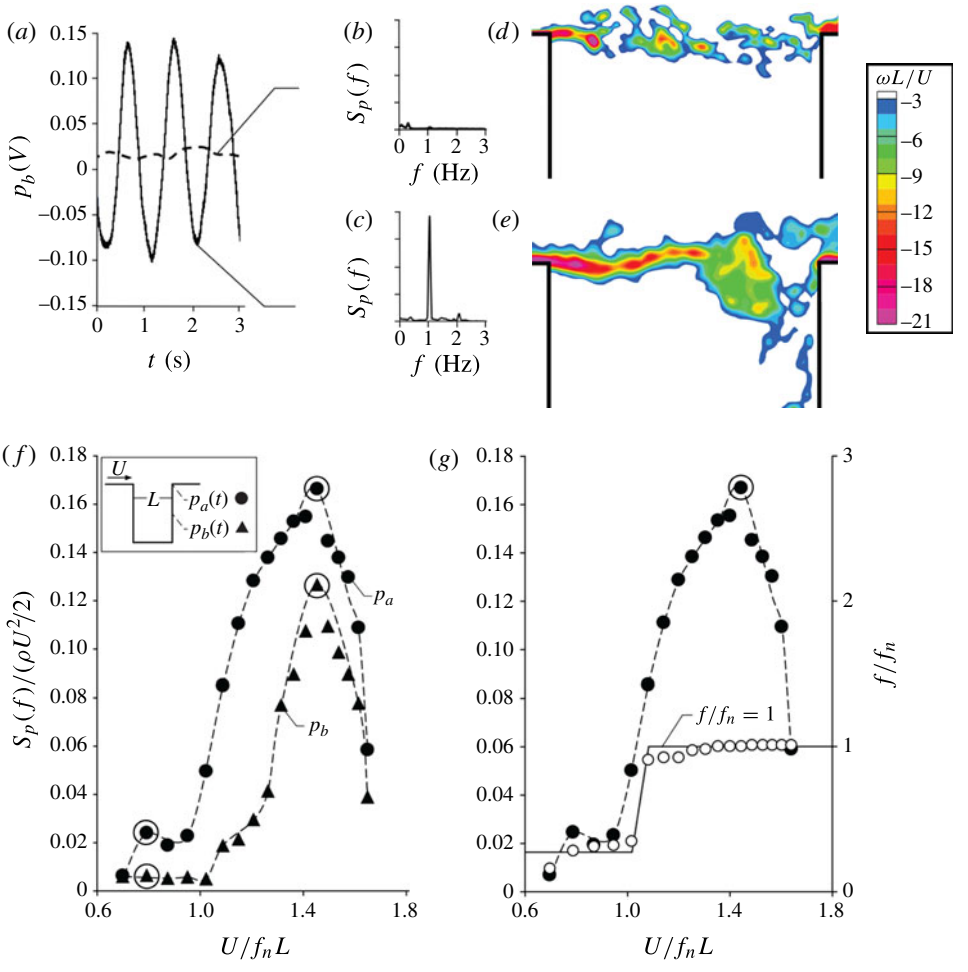


FIGURE 2. (Colour online) (*a*) Pressure signals for cases without (dashed line) and with (solid line) coupling with gravity standing wave. (*b–e*) Spectral response of pressure and instantaneous patterns of vorticity ($\omega L/U$) without and with coupling with gravity standing wave. (*f* and *g*) Amplitudes of spectral peaks $S_p(f)/(\rho U^2/2)$ of pressure and frequency f/f_n at which spectral peak of pressure fluctuation occurs as a function of dimensionless inflow velocity (U/f_nL).

fluctuations occurs at the corner. That is, in figure 2, the standing wave exists along the entire streamwise extent of the shear layer, but the conversion to vorticity fluctuations occurs at the corner.

Figure 2(*f*) shows two types of contributions to the spectral amplitudes $S_p(f)/(\rho U^2/2)$ of the pressure fluctuations within the cavity plotted against the dimensionless inflow velocity U/f_nL. The pressure p_a measured at the impingement corner indicates the combined influence of the unsteady shear layer along the cavity opening and the gravity standing wave, while the pressure p_b inside the cavity is due only to the gravity standing wave within the cavity. It is evident in figure 2(*f*) that the amplitude of the spectral peak is consistently higher for pressure p_a at the downstream corner, due to impingement of the unsteady shear layer (Tang &

https://doi.org/10.1017/jfm.2014.548 Published online by Cambridge University Press

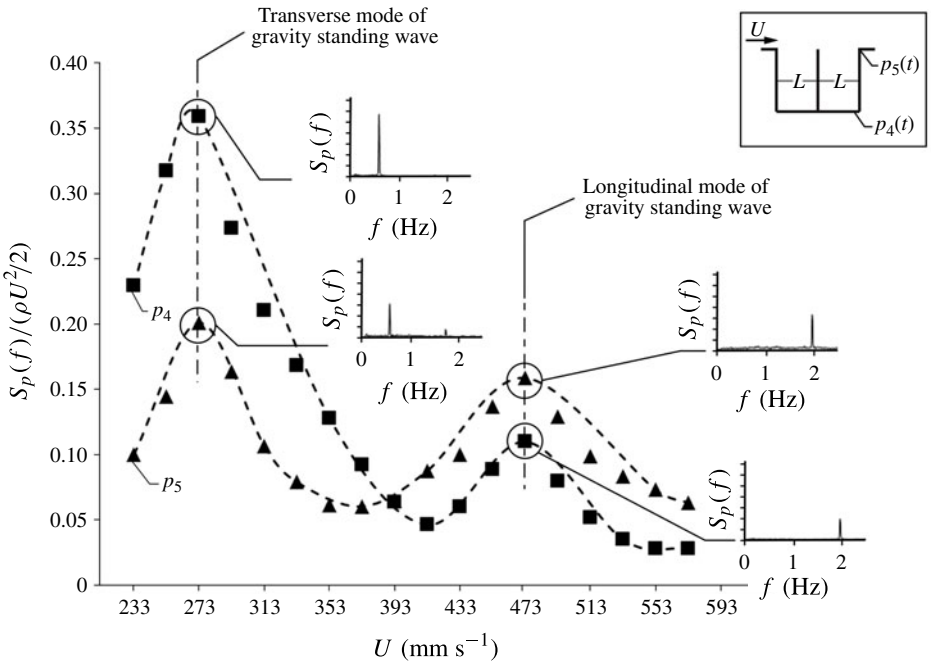


FIGURE 3. Amplitude of spectral peak $S_p(f)_{max}/(\rho U^2/2)$ as a function of the free-stream velocity U.

Rockwell 1983). For both classes of pressure fluctuations, however, very low spectral amplitudes $S_p(f)/(\rho U^2/2)$ occur at low reduced velocity, indicated by the encircled data points at $U/f_nL = 0.78$. This state of the pressure fluctuations corresponds to the case designated as no gravity standing wave in figure 2(*b*,*d*). As the value of reduced velocity U/f_nL increases, the spectral amplitudes of both p_a and p_b rise rapidly to attain a peak amplitude designated by the encircled points at $U/f_nL = 1.44$. This state of the oscillation corresponds to the maximum coupling between the inherent instability of the shear layer and the gravity standing wave, and represents the case designated as a gravity standing wave in figure 2(*c*,*e*). Further increases of U/f_nL yield rapid decreases in the spectral amplitudes of the pressure fluctuations. The fact that the resonant response of figure 2 is associated with frequency lock-on is indicated in figure 2(*g*). The locked-on state corresponds to $f/f_n = 1$, in which f_n is the eigenfrequency of the gravity standing wave in the cavity. It extends over the range of U/f_nL corresponding to large magnitude of the spectral amplitude $S_p(f)/(\rho U^2/2)$, and the largest magnitude occurs near the midpoint of the lock-on region.

4. States of resonant response: spectra and turbulence statistics

Figure 3 shows the amplitude response characteristics of the sequential cavities. This response is shown in figure 3 by the plot of dimensionless amplitude of the spectral peak of the unsteady pressure p, i.e. $S_p(f)_{max}/(\rho U^2/2)$ as a function of U. As shown in the schematic in the inset of figure 3, the pressure $p_5(t)$ measured at the impingement corner of the trailing cavity is represented by the triangular symbol, and the pressure at the end of the trailing cavity $p_4(t)$ is designated by the square symbol. The peaks in the plots of figure 3 are due to the successive onset of transverse and

https://doi.org/10.1017/jfm.2014.548 Published online by Cambridge University Press

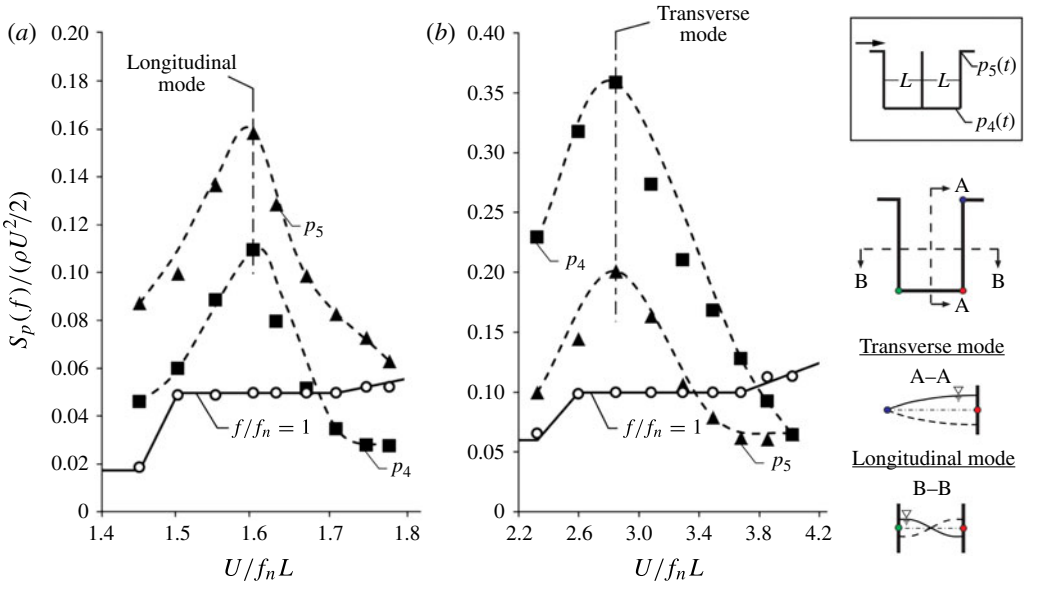


FIGURE 4. (Colour online) Amplitude of spectral peak $S_p(f)_{max}/(\rho U^2/2)$ as a function of reduced inflow velocity U/f_nL for (*a*) longitudinal and (*b*) transverse modes of gravity standing waves within cavities.

longitudinal modes of the gravity standing wave; coupling in these modes corresponds to the sharp spectral peaks in the spectra $S_p(f)$. The depth-averaged inflow velocities $U = 273$ and 475 mm s^{-1} correspond to resonant responses where the frequencies of the transverse and streamwise oriented gravity standing waves match the inherent instability frequencies of the separated shear layer as indicated in § 4.

Figure 4(*a*) gives the magnitude of the spectral peak $S_p(f)_{max}/(\rho U^2/2)$ versus U/f_nL in presence of the longitudinal (streamwise-oriented) gravity standing wave. The maximum magnitude of the spectral peak occurs at the dimensionless flow velocity $U/f_nL = 1.6$. At all values of U/f_nL, the magnitudes of the spectral peaks $S_p(f)_{max}/(\rho U^2/2)$ are consistently larger for the pressure p_5 at the impingement corner of the trailing cavity, relative to the value p_4 at the end of the cavity. For this longitudinal (streamwise-oriented) mode of the gravity standing wave, the maximum amplitudes occur along the faces of the corners and the faces of the partition wall located between the two cavities. This contribution from the standing wave, along with the contribution from the impingement of the unstable, separated shear layer upon the trailing corner, yields a larger overall unsteady pressure amplitude, relative to p_4 at the end of the cavity.

Figure 4(*b*) shows the magnitude of the spectral peak $S_p(f)_{max}/(\rho U^2/2)$ as a function of reduced velocity U/f_nL for the transverse-oriented gravity standing wave. The maximum spectral peak is attained at a value of $U/f_nL = 2.9$. It is apparent that the magnitude of the peak is consistently higher for pressure p_4 at the end of the cavity; in this transverse mode, the gravity standing wave has its maximum amplitude at the closed end of the cavity, and its minimum amplitude at the open end. There is, however, an additional contribution at the open end, arising from unsteady impingement of the unstable, separated shear layer upon the trailing corner of the cavity.

https://doi.org/10.1017/jfm.2014.548 Published online by Cambridge University Press

If the thickness of the separated shear layer is sufficiently small compared with the cavity width, as is the case for the present investigation, the instability of the separated layer along the edge of the recirculation zone can be described by linear theory. Knisely & Rockwell (1982) have demonstrated, for flow past a cavity, that the experimentally determined regions of linear (exponential amplification) growth of amplifying disturbances are well approximated using this approach. For the present investigation, in order for a locked-on oscillation to occur, the frequency of the inherent instability of the separated shear layer along the opening of the cavity must match the eigenfrequency of the gravity standing wave. Unlike the discrete eigenfrequency of the gravity standing wave, the shear layer instability can be substantially amplified over a band of frequencies, i.e. large values of amplification rate occur over a range of frequencies. In other words, any frequency within this band has the potential to match the frequency of the gravity standing wave. Since the velocity distribution across the shear layer has the form of a hyperbolic tangent, it is appropriate to use the stability theories of Michalke (1964, 1965) to determine the frequencies and wavelengths that are most susceptible for matching with the frequency of the standing wave. In fact, Chu *et al.* (1991) performed a stability analysis for disturbance growth influenced by bed friction. They replicated Michalke (1965)'s curve of amplification rate versus wavenumber of the instability wave for the limiting case of frictionless flow, that is, zero bed friction; even in the presence of increasing values of bed friction, the wavenumber associated with the maximum amplification rate changes very little, that is, by the order of 6 %. Moreover, the values of the stability parameter S determined herein are $S = 0.007$ for the transverse mode and $S = 0.004$ for the longitudinal mode of the gravity standing wave, which are present very close to the frictionless case $S = 0$. Michalke (1965) provides an overview of equivalencies between temporal and spatial disturbance amplification in terms of effective amplification rate, frequency and wavenumber. With this information, it is possible to determine the compatibility of: the eigenfrequencies of the standing waves; and the frequencies for which disturbances are highly amplified in the separated shear layer. Let the f_{tr} and f_{long} be the eigenfrequencies of the transverse (tr) and longitudinal (long) gravity standing waves. For considerations of the instability wave, these frequencies are, in dimensionless form, $f_{tr}\theta/U = 0.0124$ and $f_{long}\theta/U = 0.0179$, in which θ is the momentum thickness of the separated shear layer and U is the mainstream velocity. Considering temporal amplification, which is consistent with the plots of Chu *et al.* (1991), the values of effective amplification factor $\alpha_r\theta(c_i/c_r) = 0.09$ and 0.094, respectively, for $f_{tr}\theta/U = 0.0124$ and $f_{long}\theta/U = 0.0179$. These values of $\alpha_r\theta(c_i/c_r)$ are 94 and 97 % of the maximum value of amplification factor $\alpha_r\theta(c_i/c_r)$ that occurs at a frequency lying between the two values of aforementioned dimensionless frequency. In essence, this indicates that the frequencies in the unstable shear layer, corresponding to the eigenfrequencies of the gravity standing waves are susceptible to large amplification and thereby satisfy the essential condition for a self-sustained oscillation in the locked-on state.

Figure 5 shows spectra of the pressure fluctuation at the end of each cavity for the transverse and longitudinal modes of the gravity standing wave, corresponding respectively to values of reduced velocity $U/f_nL = 2.9$ and 1.6. The plot on the left shows the spectral response of the fluctuating pressure p_2 in the leading cavity, and the one on the right corresponds to the fluctuating pressure p_4 in the trailing cavity. It is apparent from the graphs that the frequencies of the transverse ($f_n = 0.63$ Hz) and longitudinal ($f_n = 1.96$ Hz) modes of the gravity standing wave are the same in the leading and trailing cavities, i.e. the frequency of the coupled oscillations is the

https://doi.org/10.1017/jfm.2014.548 Published online by Cambridge University Press

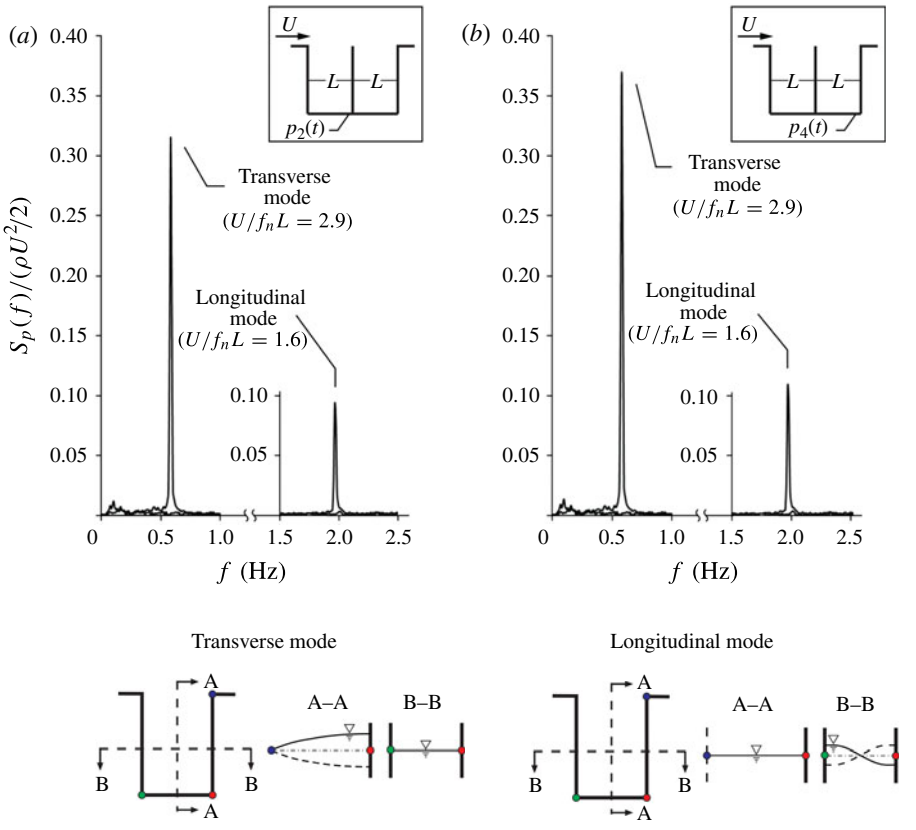


FIGURE 5. (Colour online) Amplitude of the spectral peak $S_p(f)_{max}/(\rho U^2/2)$ of pressure fluctuation in (*a*) leading and (*b*) trailing cavities for transverse and longitudinal modes of gravity standing waves within cavities.

same regardless of which cavity is considered. However, the amplitudes of the coupled oscillations are detectably different in the leading and trailing cavities. The magnitude of the spectral peak $S_p(f)_{max}/(\rho U^2/2)$ for the transverse mode is 15 % larger in the trailing (downstream) cavity, and for the longitudinal mode, it is 7 % larger in the trailing cavity.

Figures 3–5, described in the foregoing, show two resonant states arising from coupling between the unsteady shear layer along the cavity and a gravity standing wave mode within the cavity; one state involves the transverse mode and the other involves the longitudinal (streamwise-oriented) mode of the gravity standing wave. In these resonant states, the spectra S_v/U of the transverse v component of the velocity fluctuation in the unsteady separated shear layer along the opening ($y = 0$) of each cavity have the forms indicated in figure 6. The maximum value of the spectral peak S_v/U is significantly larger for the transverse mode of the gravity standing wave. Irrespective of whether the transverse or longitudinal mode is considered, sharply defined spectral peaks are evident in the leading and trailing cavities.

Figure 7 shows an overview of the patterns of: root-mean-square (r.m.s.) of the streamwise (longitudinal) velocity fluctuation u_{rms}/U (top row), transverse (vertical) velocity fluctuation v_{rms}/U (middle row) and Reynolds shear stress $\langle u'v'\rangle/U^2$ (bottom

https://doi.org/10.1017/jfm.2014.548 Published online by Cambridge University Press

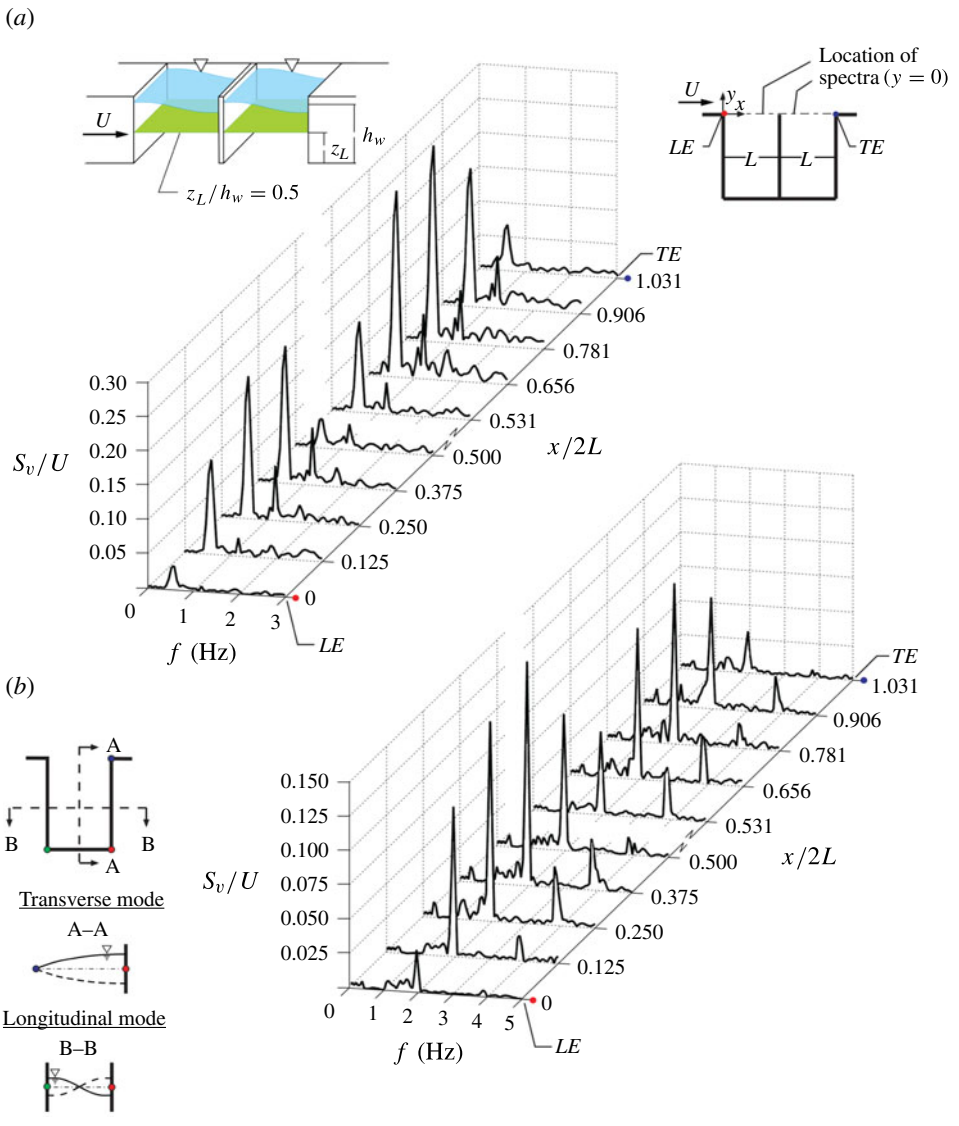


FIGURE 6. (Colour online) Spectra S_v/U of cross-stream velocity fluctuation in shear layer along openings of cavities ($y = 0$), for transverse (a) and longitudinal (b) modes of gravity standing waves within cavities.

row). For the case of the transverse-oriented gravity standing wave at $U/f_nL = 2.9$ in figure 7(a), it is evident that the spatial extent and the peak magnitude of each of the aforementioned turbulence quantities are larger for the trailing cavity of the two cavity system. To be sure, substantial amplitudes occur along the leading cavity. A further distinction is that the regions of largest (dark red) magnitude tend to occur in the upstream region of the separated shear layer of the trailing cavity. These largest-magnitude regions along the opening of the trailing cavity are apparently due to the downstream propagation of turbulence within the separated shear layer. Regarding the longitudinal (streamwise-oriented) gravity standing wave,

https://doi.org/10.1017/jfm.2014.548 Published online by Cambridge University Press

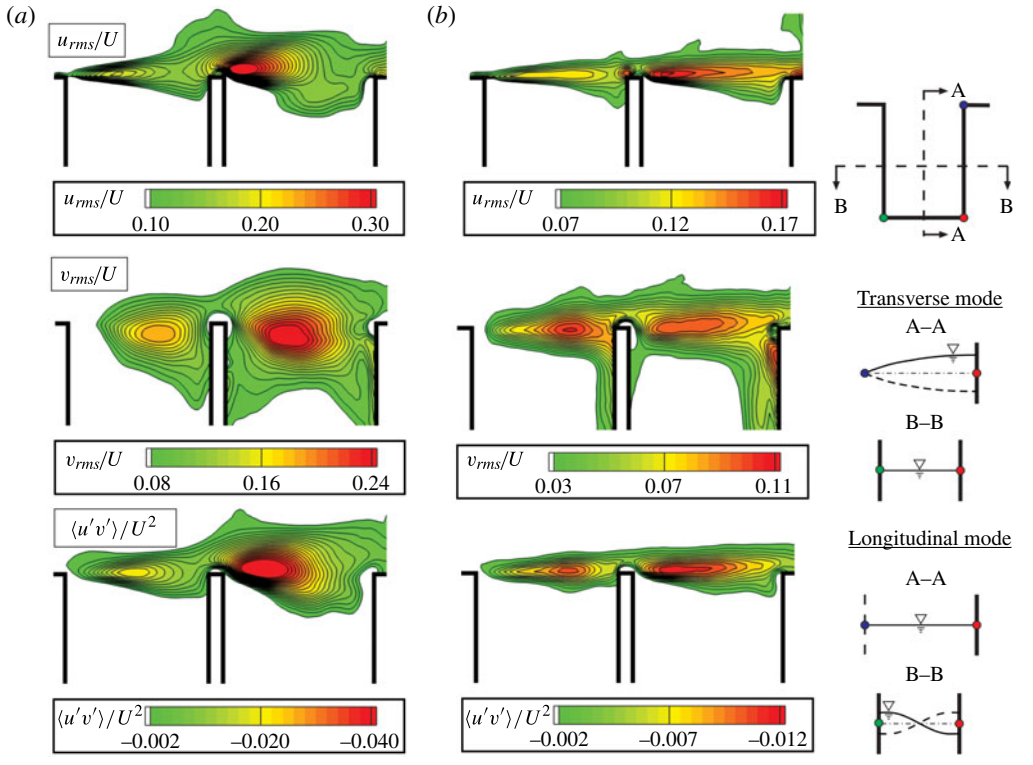


FIGURE 7. (Colour online) Patterns of r.m.s. of the streamwise (u_{rms}/U) and transverse (v_{rms}/U) velocity fluctuations, Reynolds stress $\langle u'v'\rangle/U^2$, for transverse and longitudinal modes of gravity standing waves within cavities, are represented respectively by images in (*a*) and (*b*).

the corresponding images in the right column of figure 7 indicate larger magnitudes of all turbulence quantities in the early region of development of the shear layer along the trailing cavity relative to the leading cavity. A common feature of all of the images of figure 7 is therefore enhanced levels of streamwise u_{rms}/U and transverse v_{rms}/U fluctuations and Reynolds stress $\langle u'v'\rangle/U^2$ in the initial region of development of the separated shear layer along the trailing cavity. This observation suggests that the unsteadiness from the shear layer along the leading cavity and its interaction with the impingement corner of the leading cavity provide unsteady inflow conditions for the shear layer along the trailing cavity. This incident unsteadiness either modulates or interacts with the naturally evolving unsteadiness of the trailing shear layer to yield the enhancements of the turbulence quantities evident in figure 7. The associated fluctuations for both the transverse and longitudinal cases of figure 7 show well-defined concentrations of v_{rms}/U, which are different in magnitude, as evidenced by the velocity spectra of figure 6. Moreover, the existence of a V-shaped amplification of u_{rms}/U (top row) is present in both cases, which was also detected by Ekmekci & Rockwell (2007, 2010), Basley *et al.* (2011), Liu & Katz (2011) and Tuna *et al.* (2013). These patterns of u_{rms}/U are due to the onset and streamwise growth of the instability and turbulence in the separated shear that forms downstream of flow separation, which occurs at the corner of the cavity. That is, when the shear layer separates, an inflection point appears in its velocity distribution; this inflectional

https://doi.org/10.1017/jfm.2014.548 Published online by Cambridge University Press

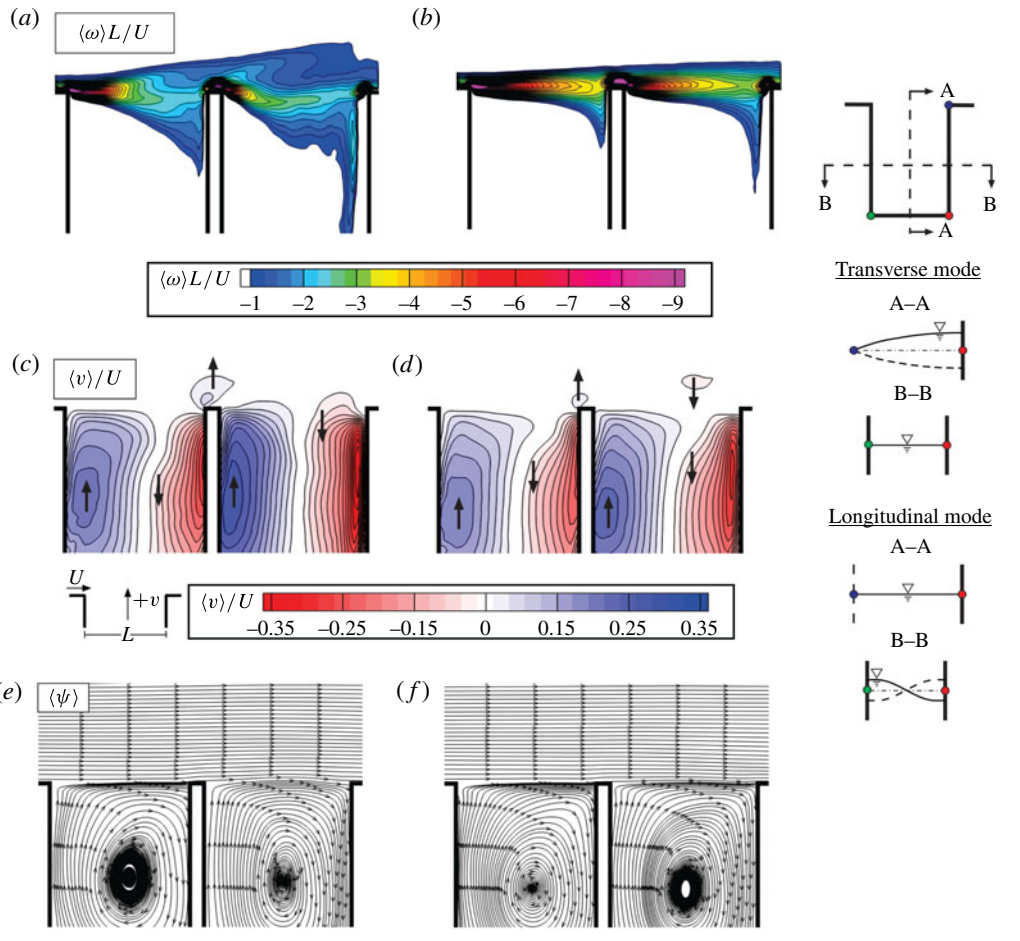


FIGURE 8. (Colour online) (*a*,*b*) Contours of time-averaged vorticity $\langle\omega\rangle L/U$; (*c*,*d*) transverse velocity $\langle v\rangle/U$; and (*e*,*f*) streamlines $\langle\psi\rangle$, for transverse and longitudinal modes of gravity standing waves within cavities, are represented respectively by images in (*a*,*c*,*e*) and (*b*,*d*,*f*).

distribution promotes the rapid amplification of disturbances and enhancement of turbulence. Patterns of u_{rms}/U can show V-shaped amplification both with and without existence of a gravity standing wave within the cavity, as shown in the shallow flow investigations of Ekmekci & Rockwell (2007) and Tuna *et al.* (2013).

5. Time-averaged flow structure

Figure 8 provides time-averaged representations of the flow structure. In figure 8(*a*), contours of time-averaged vorticity $\langle\omega\rangle L/U$ indicate a wide extent of $\langle\omega\rangle L/U$, which is consistent with the large magnitudes of the turbulence quantities u_{rms}/U, v_{rms}/U and $\langle u'v'\rangle/U^2$ in the presence of the transverse mode of the gravity standing wave given in figure 7. Moreover, when the longitudinal (streamwise-oriented) gravity standing wave exists, as shown in figure 8(*b*), the width of the vorticity layer $\langle\omega\rangle L/U$ is substantially diminished. The rate of attenuation of high levels of $\langle\omega\rangle L/U$ in the streamwise direction is also of interest. For the longitudinal mode of the standing

https://doi.org/10.1017/jfm.2014.548 Published online by Cambridge University Press

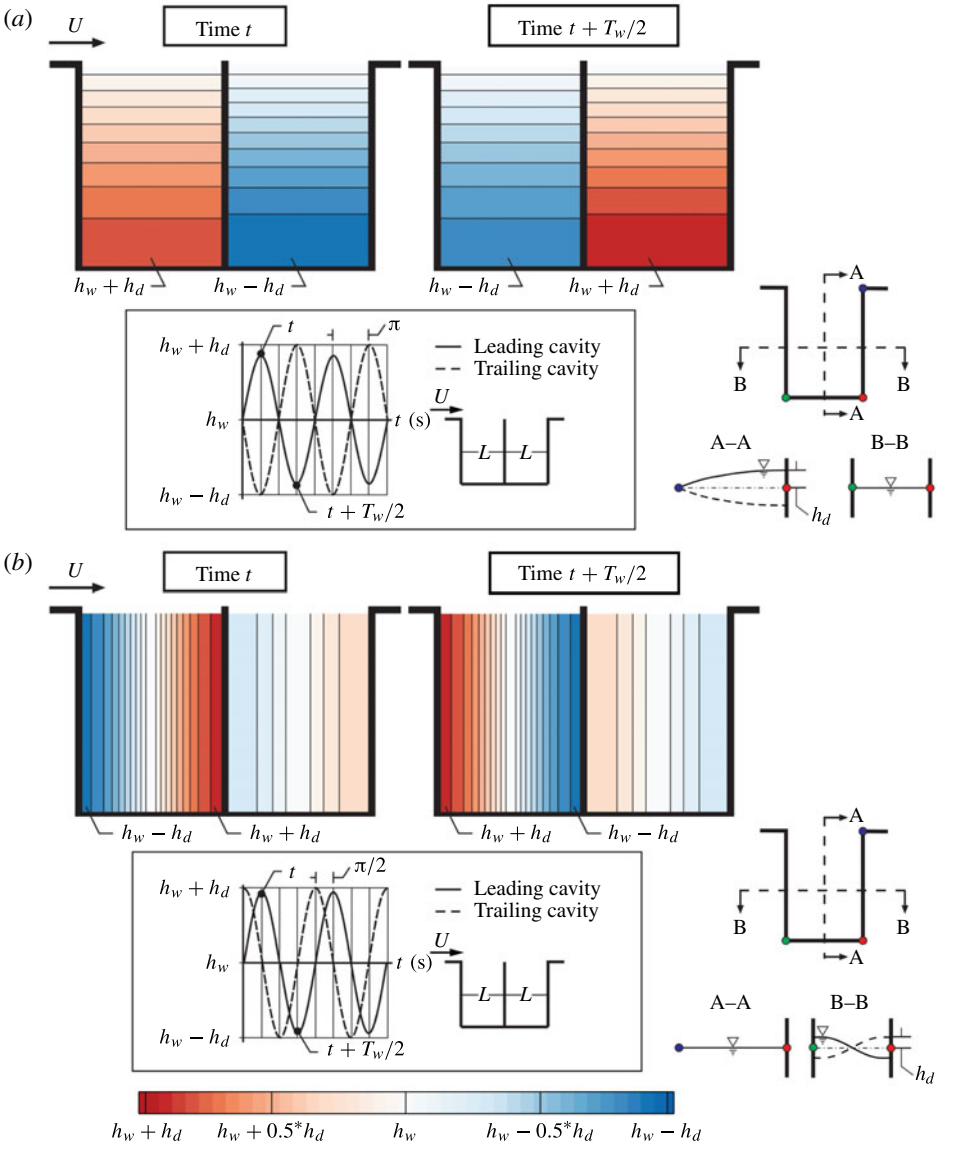


FIGURE 9. (Colour online) Contours of instantaneous water depth inside cavity corresponding to transverse (*a*) and longitudinal (*b*) modes of gravity standing waves within cavities. Red contour levels represent values of water depth larger than the nominal water depth h_w and blue contour levels represent values of water depth smaller than nominal depth h_w; h_d is oscillation amplitude of gravity standing wave.

wave, the (yellow) region that indicates a high level of vorticity $\langle\omega\rangle L/U$ extends well downstream towards the impingement region of each cavity. On the other hand, for the transverse mode of the gravity standing wave, the high levels (yellow colours) of $\langle\omega\rangle L/U$ are rapidly attenuated in the streamwise direction. It is therefore evident that the magnitudes of the aforementioned turbulent stresses in the separated shear layer along the cavity opening are directly correlated to both the rate of degradation of peak vorticity and increase in width of the time-averaged vorticity layer.

https://doi.org/10.1017/jfm.2014.548 Published online by Cambridge University Press

Figure 8(*c*,*d*) show contours of constant time-averaged transverse velocity $\langle v \rangle / U$. Blue contours indicate outward-oriented transverse flow, i.e. flow towards the opening of the cavity, and red contours indicate inward-oriented flow, that is, into the cavity. Larger magnitude, outward-oriented (dark blue) flow and inward-oriented (dark red) flow occurs for the transverse mode figure 8(*c*), relative to the longitudinal mode figure 8(*d*), thereby signifying enhanced recirculation flow within the cavity for the transverse mode. A further, common feature of both cases is the existence of a localized region of outward-oriented flow at the upstream corner of the splitter plate, i.e. impingement corner of the leading cavity. However, the scale of this localized region decreases in presence of the longitudinal gravity standing wave. Consideration of this localized blue cluster in conjunction with the red contours along the upstream edge of the splitter plate (trailing edge of the leading cavity) suggests a stagnation point near the upstream corner of the splitter plate, i.e. the impingement corner of the leading cavity.

Figure 8(*e*,*f*) show patterns of time-averaged streamlines $\langle \psi \rangle$. Both of these patterns show existence of a stagnation streamline, which emanates from the upstream corners of the leading and trailing cavities and impinges on the respective downstream corners. Remarkably, the general form of the streamline patterns is very similar for the cases of transverse and longitudinal modes of the gravity standing waves within the cavities and, furthermore, for both the leading and trailing cavities in a given mode. Furthermore, for both modes of the gravity standing wave, there is a single large recirculating eddy within the cavity, which has an aspect ratio $L/W = 0.66$. This pattern is also evident in the review of Shankar & Deshpande (2000) for lid driven cavities having aspect ratios L/W of 0.5 and 1. Immediately exterior to the region surrounding the foci (centres) of the streamline patterns, the streamline pattern spirals outward in all cases.

6. Phase-averaged flow structure

An understanding of the origin of the strongly coupled resonant states described in the foregoing requires consideration of the time sequence of patterns of the flow structure along and within the cavity, with particular attention to: (i) a favourable phase shift between the standing waves that occur in the leading and trailing cavities of the two-cavity system; and (ii) an overall phase shift of the transverse undulations of the separated shear layer along the opening of each cavity as well as along the entire extent of the system of successive cavities. In the following, the phase shift between the gravity standing waves in adjacent cavities is first addressed, followed by the phase shift along the separated shear layer.

Highly coherent oscillations of the nominally turbulent shallow flow past the sequence of cavities are attainable through coupling with gravity standing wave modes within the cavities. The gravity standing wave mode that exists within a given cavity, and its phase relationship to the mode in the adjacent cavity, are central to determining whether a self-excited coherent oscillation occurs. Figure 9 shows the admissible modes and phase relationships of the gravity standing wave systems, which were determined during self-sustained oscillations from multiple pressure measurements on the walls of the cavities, at the locations (p_1, p_2, p_3, p_4) indicated in figure 1. The elevation of the free surface above the bed (bottom surface), that is, the water depth, is designated by shades of red and blue, where red indicates a water depth larger than the nominal water depth h_w, and blue corresponds to a depth smaller than the nominal value h_w. The vertical displacement h_d corresponds

https://doi.org/10.1017/jfm.2014.548 Published online by Cambridge University Press

to the amplitude of the free surface oscillation within the cavity, and the extreme amplitudes are designated as $h_w \pm h_d$. For both sets of schematics shown in figure 9, the instantaneous elevation of the free surface is shown at a defined time t and a later time $t + T_w/2$, in which T_w is the period of oscillation of the gravity standing wave. The plots of h_w versus t in figure 9 illustrate the time history of free surface elevation over two oscillation periods, i.e. $2T_w$. In these plots, the solid and dashed lines correspond respectively to the time-dependent elevations of the free surface in the leading and trailing cavities.

The top row of schematics of figure 9 shows the existence of a transverse gravity standing wave in each cavity; these gravity standing waves are shifted by a phase angle of π (180°). At the instants of time t and $t + T_w/2$, the gravity standing wave in the trailing cavity is shifted by π with respect to the gravity standing wave in the leading cavity. This phase difference of π is, of course, maintained for all values of t as shown in the graph. For the images shown in the top row of figure 9, the (red) free-surface elevation in the leading cavity at time t is larger than the nominal elevation h_w of the free surface, while at time $t + T_w/2$ the (blue) free-surface elevation in the leading cavity is smaller than the nominal elevation of h_w.

The bottom row of schematics represents the gravity standing waves in the longitudinal (streamwise-oriented) mode in both sequential cavities; they are shifted with respect to each other by $\pi/2$, that is, the phase angle between them is 90°. At time t, in the region along the left boundary of the leading cavity, the elevation (blue) of the free-surface is smaller than the nominal elevation h_w. At time $t + T_w/2$, this same region of the free surface has an elevation (red) greater than the nominal depth h_w. At both instants of time, the elevation of the free surface in the trailing cavity is approximately at the nominal elevation h_w, which shows the $\pi/2$ phase shift of the gravity standing wave between two cavities. For both the transverse and longitudinal modes described in the foregoing, the unique value of phase shift that occurs between the gravity standing waves in adjacent cavities indicates that the oscillation of the two cavity system is a globally coupled phenomenon.

The foregoing patterns of phase shifted gravity standing waves in successive cavities coexist with the separated vorticity layers along the openings of the cavities. Figure 10(*a*,*b*) show patterns of phase-averaged vorticity $\langle\omega\rangle_p L/U$ for the transverse and longitudinal modes of the gravity standing waves. By comparison of images at a given phase, it is possible to determine common features of the vortical structures in the separated shear layers. Clusters of phase-averaged vorticity are labelled as A, B, C and D. In figure 10(*a*), at $\phi = 0°$, the clusters of $\langle\omega\rangle_p L/U$ in the leading and trailing cavities are labelled as *A* and *B*. Similar clusters of vorticity can be identified at $\phi = 180°$; however, at this value of ϕ, cluster B is in the leading cavity and cluster A is in the trailing cavity as a result of π phase shift between the gravity standing waves in the leading and trailing cavities. A similar comparison can be done at the oscillation phases of $\phi = 90$ and 270°; where clusters of phase-averaged vorticity are labelled as C and D. On the other hand, in figure 10(*b*), like clusters of vorticity occur at different phases. At $\phi = 180°$, the vorticity cluster along the leading cavity is labelled as C. A similar cluster C is evident along the trailing cavity at $\phi = 270°$, due, of course, to the $\pi/2$ phase shift between leading and trailing cavities. This phase shift can also be seen by comparing clusters of vorticity A, B and D at different phase angles ϕ of the oscillation.

Furthermore, it is possible to determine the consequence of different orientations of the gravity standing wave on the patterns of Reynolds stress correlation $\langle u'v'\rangle/U^2$ in figure 7 by cross-comparison of the patterns of phase-averaged vorticity in

https://doi.org/10.1017/jfm.2014.548 Published online by Cambridge University Press

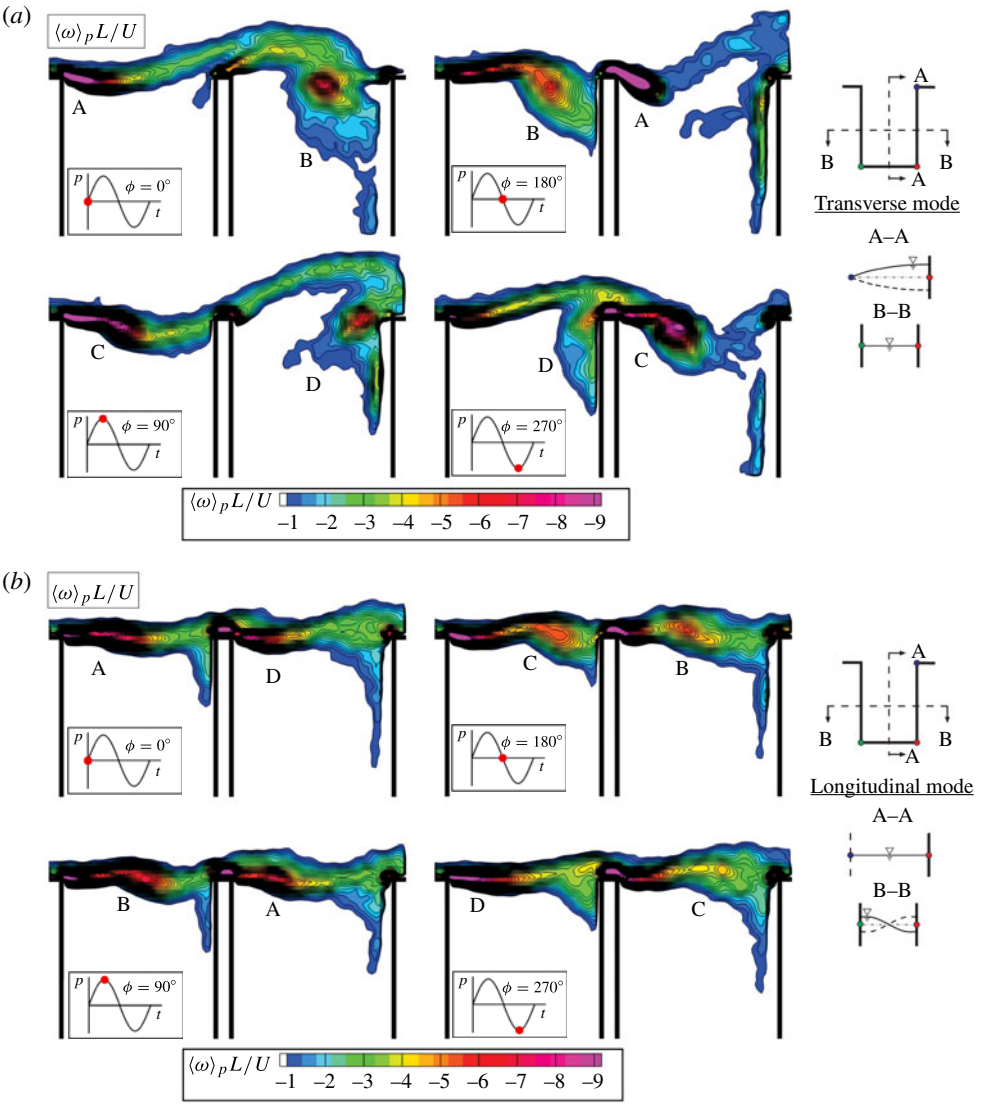


FIGURE 10. (Colour online) (*a*) Contours of phase-averaged vorticity $\langle\omega\rangle_p L/U$, for transverse mode of gravity standing wave within cavities. (*b*) Contours of phase-averaged vorticity $\langle\omega\rangle_p L/U$, for longitudinal mode of gravity standing wave within cavities.

figure 10(*a*,*b*). For the transverse mode of the gravity standing wave in figure 10(*a*), large-amplitude transverse excursions of the vorticity layer occur over an oscillation cycle. On the other hand, in figure 10(*b*) for the longitudinal standing wave, the vorticity layer shows smaller-amplitude transverse excursions about a nominal state. These observations are consistent with the patterns of Reynolds stress correlation $\langle u'v'\rangle/U^2$ given in figure 7.

Another crucial element of the resonant, self-sustained oscillations described in the foregoing is the transverse undulation of the separated vorticity layer along the opening of the cavity, represented by the transverse velocity component $v(t)$. Its streamwise phase variation $\Phi_v(x)$ is central to determination of the phase speed and

https://doi.org/10.1017/jfm.2014.548 Published online by Cambridge University Press

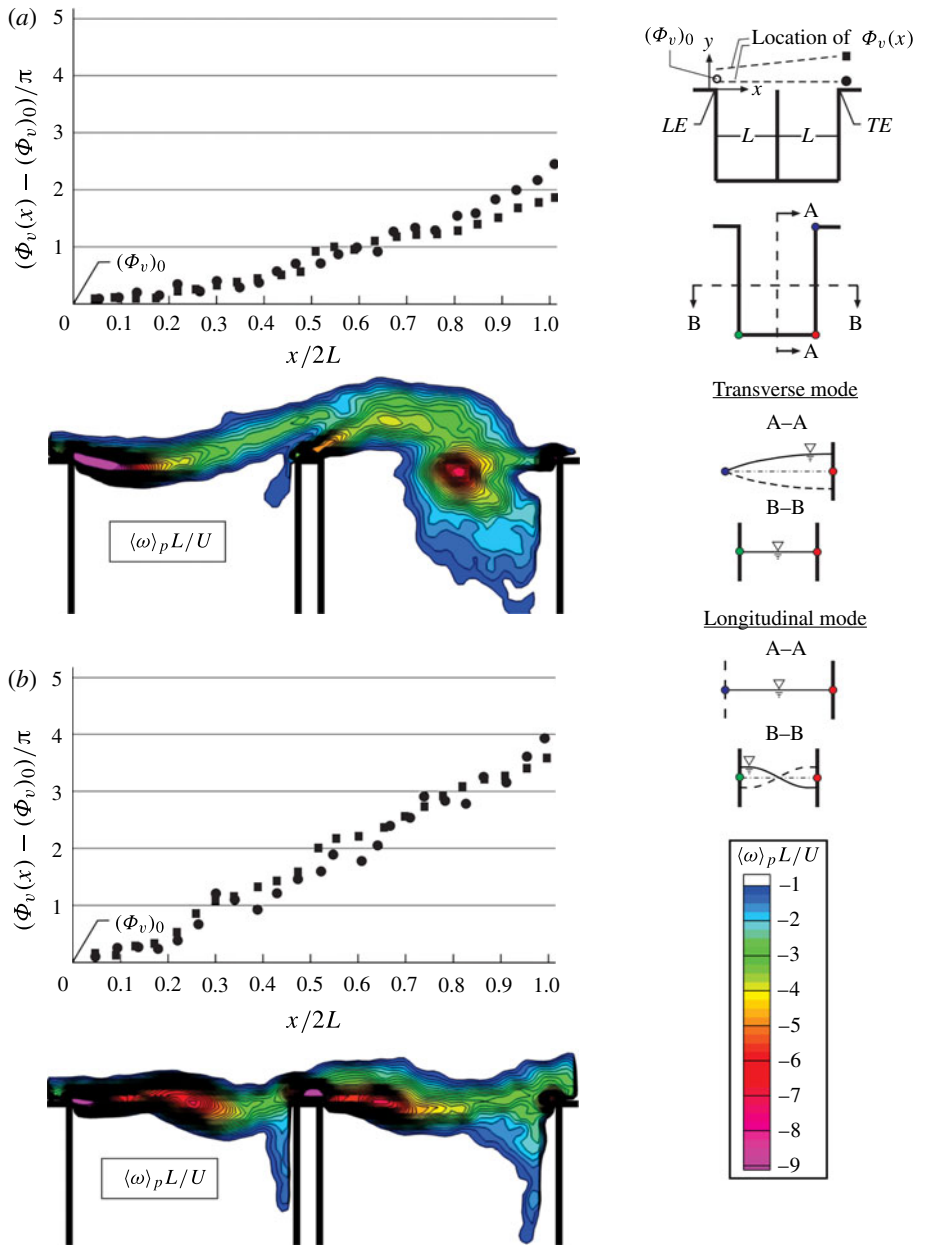


FIGURE 11. (Colour online) Phase variation of transverse velocity Φ_v with downstream position $(x/2L)$ along a horizontal line $y/L = 0.08$ (circular symbols) and along a line where $\langle u\rangle/U = 0.9$ (square symbols), for transverse (a) and longitudinal (b) modes of gravity standing waves within cavities.

wavelength. Figure 11 shows the streamwise phase variation $[\Phi_v - (\Phi_v)_0]/\pi$, in which $(\Phi_v)_0$ is the phase angle at the separation corner. Two paths were employed for evaluation of $[\Phi_v - (\Phi_v)_0]/\pi$: along a horizontal line at an elevation of $y/L = 0.08$ (circular symbols) above the leading corner of the sequential cavity configuration; and along a line at the edge of the time-averaged velocity distribution where $\langle u\rangle/U = 0.9$

https://doi.org/10.1017/jfm.2014.548 Published online by Cambridge University Press

(square symbols). Also shown is a representative image of contours of constant vorticity at a selected instant during the oscillation cycle. For the case of the gravity standing wave oriented in the transverse direction, represented by the top plot, the value of $[\Phi_v - (\Phi_v)_0]/\pi$ increases with streamwise distance $x/2L$. Particularly remarkable is that the overall phase difference is $[\Phi_v - (\Phi_v)_0]/\pi \cong 2$ from the separation corner of the leading cavity at $x/2L = 0$ to the impingement corner of the trailing cavity at $x/2L = 1$. Deviations from an exact value of $[\Phi_v - (\Phi_v)_0]/\pi = 2$ are due to the end condition at impingement, that is, distortion of the vorticity layer as it approaches the impingement corner. Furthermore, the overall form of the pattern of vorticity, which extends over the leading and trailing cavities, mimics very closely formation of a single vortex. For the case of incompressible flow past a single cavity in the absence of free-surface and gravity standing wave effects, it is known that formation of a single vortex along the cavity opening is associated with an overall phase difference along the separated vorticity layer of 2π (Knisely & Rockwell 1982). In other words, due to the phase difference of π between the transverse gravity standing waves in the leading and trailing cavities of the transverse mode of figure 11, and an overall phase difference of 2π of the undulating shear layer, it is possible to attain a vorticity layer resembling a single large-scale vortex, at least during a portion of the oscillation cycle, thereby mimicking the classical oscillation past a single cavity.

On the other hand, for the case of the longitudinal mode given in figure 11, the overall phase difference is $[\Phi_v - (\Phi_v)_0]/\pi \cong 4$ from the separation corner of the leading cavity at $x/2L = 0$ to the impingement corner of the trailing cavity at $x/2L = 1$, with approximately 2π phase difference along the leading cavity and 2π phase difference along the trailing cavity. Such a phase difference of 2π along each of the cavities allows the oscillation along each cavity to be self-sustained. The corresponding vorticity image indicates an organized, undulating disturbance along each cavity. The structure of the vorticity layer is representative of a low-amplitude undulating disturbance that apparently is reinforced through the condition of a 2π phase shift between perturbations at the leading-edge of the leading cavity and the tip of the partition between the two cavities.

Physical interpretation of the overall phase difference of $2n\pi$, $n = 1, 2, \ldots$, in the streamwise direction in the undulating vorticity layer, described in the foregoing has been addressed for the case of a single cavity configuration, in the absence of a free surface, by Rockwell & Naudascher (1979), Knisely & Rockwell (1982) and Rockwell (1983). Upstream influence arising from impingement of the undulating vorticity layer upon the trailing (downstream) corner of the cavity induces vorticity fluctuations in the highly receptive region of shear layer separation at the leading (upstream) corner of the cavity. When the overall phase difference of the downstream traveling wave associated with the undulating vorticity layer has a value of $2n\pi$, $n = 1, 2, \ldots$, this effect of the upstream influence is reinforced to provide a self-sustaining feedback loop, and therefore a highly coherent oscillation. This same concept can be applied to the present case of sequential cavities, for both the foregoing cases of the transverse and longitudinal gravity standing waves.

Complementary insight into the cavity oscillations is provided in figure 12; it shows the contours of constant phase-averaged transverse velocity $\langle v \rangle_p/U$ over an oscillation cycle. The colour red indicates a direction of transverse velocity oriented in the negative vertical direction, that is, into the cavity, whereas colour blue indicates an orientation in the opposite direction. These patterns provide a basis for interpretation of the flow structure associated with both the vorticity and non-vorticity bearing regions of the flow.

https://doi.org/10.1017/jfm.2014.548 Published online by Cambridge University Press

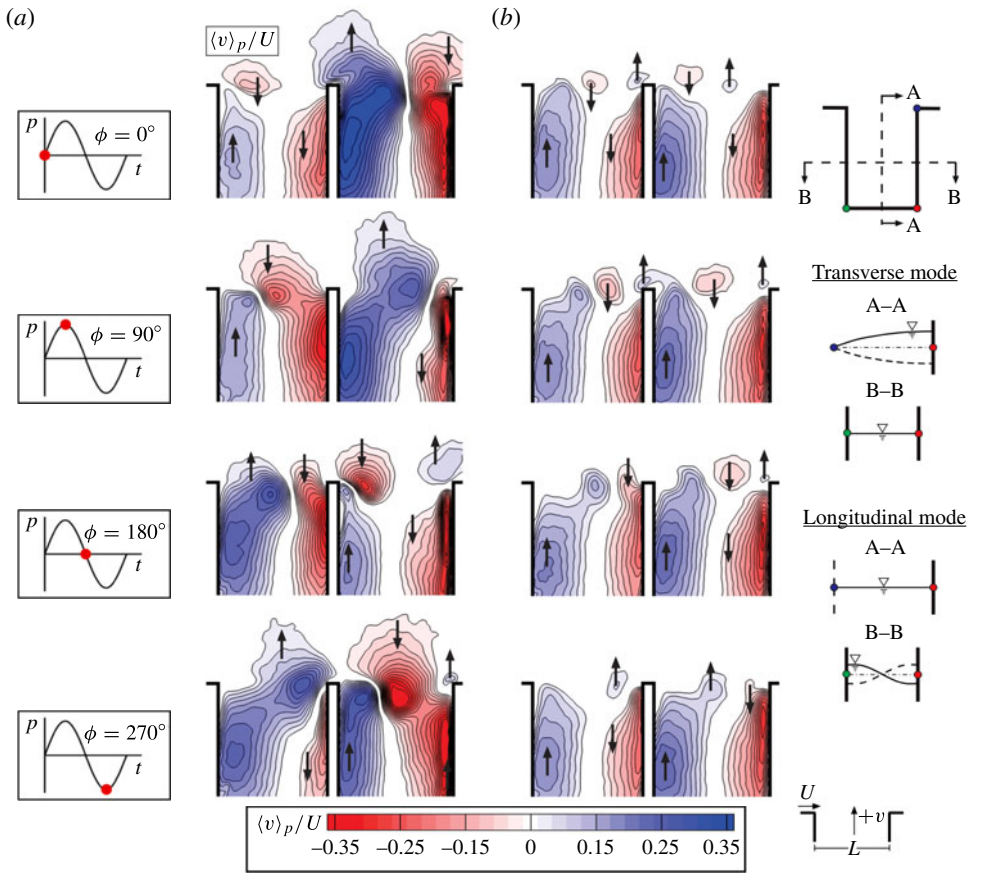


FIGURE 12. (Colour online) Contours of phase-averaged transverse velocity $\langle v\rangle_p/U$, for transverse and longitudinal modes of gravity standing waves within cavities, are represented respectively by images in (*a*) and (*b*).

Consider first the transverse mode, i.e. the left column of images. In the first two rows of images of figure 12, that is $\phi = 0$ and 90°, outward-oriented (blue contours) flow dominates along the mouth of the trailing cavity, and inward-oriented (red contours) flow is prevalent along the mouth of the leading cavity. Due to the π phase shift between the leading and trailing cavities, these patterns are switched at larger values of phase angle ϕ of the oscillation. That is, if the patterns at $\phi = 90$ and 270° are compared, the patterns of $\langle v\rangle_p/U$ are switched between the leading and trailing cavities. For example, the red and blue contour patterns appearing in the leading cavity at $\phi = 90°$ are located in the trailing cavity at $\phi = 270°$. Likewise, the contour patterns appearing in the trailing cavity at $\phi = 90°$ are approximately replicated in the leading cavity at $\phi = 270°$. The contributions to the patterns of $\langle v\rangle_p/U$ are from the motion of the inviscid gravity standing wave, vorticity bearing fluid in the large-scale recirculation zone within the cavity, as well as vorticity bearing fluid in the separated shear layer along the opening of the cavity. Despite these different contributions, the phase shift of π between the gravity standing waves in the leading and trailing cavities is maintained in the patterns of $\langle v\rangle_p/U$.

The longitudinal mode of the gravity standing wave is represented in the right column of figure 12. The patterns of the gravity standing wave given in figure 9

https://doi.org/10.1017/jfm.2014.548 Published online by Cambridge University Press

indicate a phase shift of $\pi/2$ between the leading and trailing cavity, in absence of the vorticity field associated with the recirculation within the cavity and the separated layers along the cavity openings. This phase shift is reflected in the patterns of figure 12. For example, the patterns of transverse velocity $\langle v\rangle_p/U$ in the leading cavity at $\phi = 90°$, are very similar to those in and along the trailing cavity at $\phi = 180°$.

For both the transverse and longitudinal modes of the gravity standing wave, represented by the patterns in the left and right columns of figure 12, well-defined red and blue concentrations exist along the cavity opening. Generally speaking, there is a correlation between the centre of the vorticity concentrations given in figure 10(*a*,*b*) and the location midway between the centres of a given pair of concentrations of $\langle v\rangle_p/U$ in figure 12. Moreover, these pairs of $\langle v\rangle_p/U$ concentrations propagate downstream along the opening of a given cavity. In turn, this propagation (or phase) speed c_v/U is related to the streamwise variations of phase $[\Phi_v - (\Phi_v)_0]/\pi$ along the cavity opening, given in figure 11. That is, $c_v/U = 2\pi f/(\partial\Phi/\partial x)U$. It is evident from the plots of $[\Phi_v - (\Phi_v)_0]/\pi$ given in figure 11 that the variation of $[\Phi_v - (\Phi_v)_0]/\pi$ with $x/2L$ is nonlinear in the region immediately downstream of the separation corner of the leading cavity, that is, the slope of this curve is small, and thereby the phase speed will be correspondingly small. The averaged phase speed was calculated over the openings of the leading and trailing cavities, that is, extending from $x/2L = 0$ to 1. The values are $c_v/U = 0.70$ and 0.63, respectively, for the transverse and longitudinal wave systems within the cavities. In addition, it is possible to deduce the averaged wavelength λ/L along the leading and trailing cavities according to the relationship c_v/f. For the transverse and longitudinal modes of gravity standing wave, these values are $\lambda/L = 2$ and 1, respectively, thereby reinforcing the observations in the foregoing that the transverse mode of the gravity standing wave is associated with approximately one wavelength extending over the openings of the leading and trailing cavities, and thereby the tendency to form a single large-scale vortex. On the other hand, for the case of the longitudinal modes within the leading and trailing cavities, one wavelength exists along each of the cavities.

Phase-averaged streamline $\langle\psi\rangle_p$ patterns are given in figure 13. It is evident that the magnitude of the undulation of the interface between the mainstream and the cavity is larger in presence of the transverse gravity standing waves, shown in the left column of images, relative to the longitudinal mode of the gravity standing waves, represented in the right column of images. Furthermore, for the transverse mode, the π phase shift between the oscillations of adjacent cavities is apparent. For example, at $\phi = 90°$ (second row), in the trailing cavity, the streamline patterns at the interface with the mainstream and in the recirculation zone exhibit similarity with the patterns in the leading cavity at $\phi = 270°$ (fourth row) due to the π phase shift between the transverse gravity standing waves in these cavities. Likewise, for the longitudinal gravity standing wave system (right column of images), the deformation of the streamlines at the interface of the leading cavity at $\phi = 90°$ is similar to that along the downstream cavity at $\phi = 180°$. Moreover, the overall streamline pattern and the location of the focus (centre) of the pattern is very similar for these two cases. These observations are indicators of the $\pi/2$ phase shift between leading and trailing cavities, which are directly linked to the phase shift between the longitudinal gravity standing waves within these cavities.

The streamline $\langle\psi\rangle_p$ patterns of figure 13 reveal an additional feature involving the interaction of the flow fields between the leading and trailing cavities. Consider the pattern at $\phi = 270°$ for the transverse standing wave (left column). It is possible to identify streamlines, emanating from the interior of the leading cavity, and over the

https://doi.org/10.1017/jfm.2014.548 Published online by Cambridge University Press

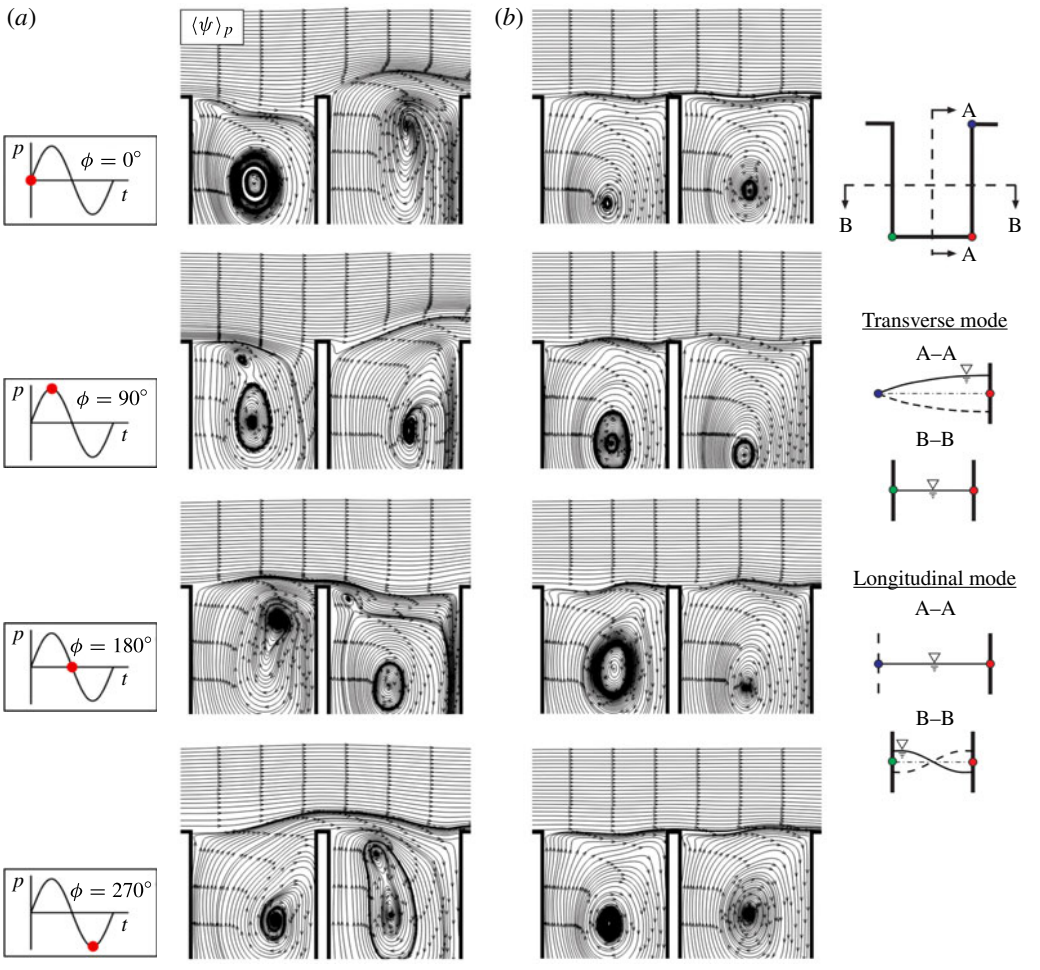


FIGURE 13. (Colour online) Patterns of phase-averaged streamlines $\langle\psi\rangle_p$, for transverse and longitudinal modes of gravity standing waves within cavities, are represented respectively by images in (*a*) and (*b*).

partition between the leading and trailing cavity. Then, these streamlines are deflected into the interior of the trailing cavity, more specifically, along its impingement wall. Thus, the large amplitude oscillations in the transverse mode, involve mass exchange between the leading and trailing cavities during part of the oscillation cycle. At later times, corresponding to values of phase angle $\phi = 0$, 90 and 180°, the leading cavity shows a stagnation point in the impingement region. With increasing values of ϕ, the stagnation point migrates upward until, at $\phi = 270°$, a gap is created, which allows flow to pass into the trailing cavity. This mass exchange is therefore limited to a relatively small window of ϕ during the oscillation cycle. On the other hand, for the longitudinal gravity standing wave mode, represented in the right column of figure 13, the patterns of $\langle\psi\rangle_p$ indicate that the stagnation point at impingement in the leading cavity remains at the corner of the impingement surface.

https://doi.org/10.1017/jfm.2014.548 Published online by Cambridge University Press

7. Time-averaged patterns of mass exchange

All of the foregoing patterns of the flow structure have important consequences for the patterns of mass exchange between the mainstream and the cavity. A dimensionless mass exchange coefficient k can be calculated along the cavity openings; it reveals the effects of orientation of the gravity standing wave on the mass exchange process. The dimensionless mass exchange coefficient is evaluated as

$$k = \frac{\overline{E(t)}}{2U}, \tag{7.1}$$

in which $\overline{E(t)}$ is the time-averaged exchange velocity and U is the free-stream velocity.

A total of 3000 randomly acquired instantaneous velocity vector fields were averaged to calculate time-averaged values of $\overline{E(t)}$, which is given as

$$\overline{E(t)} = \frac{1}{L}\int_0^L |v(t)|\,\mathrm{d}x, \tag{7.2}$$

where $v(t)$ is the instantaneous cross-stream (transverse) velocity along the cavity opening and L is the length of the cavity. Details of formulation of the exchange velocity and mass exchange coefficient are given by Tuna *et al.* (2013).

Figure 14 shows the time-averaged exchange velocity $\overline{E(t)}$ distribution along the cavity openings together with the patterns of Reynolds stress correlation $\langle u'v'\rangle/U^2$. The plot at the top represents the transverse mode ($U/f_nL = 2.9$) of the gravity standing wave, and the one at the bottom provides the longitudinal mode ($U/f_nL = 1.6$). It is clear that the overall magnitude of $\overline{E(t)}$ along the cavity opening is significantly larger in presence of the transverse mode of the gravity standing wave. Furthermore, a comparison of the $\overline{E(t)}$ trends between the leading (upstream) and the trailing (downstream) cavities reveals the relation between the Reynolds stress patterns and mass exchange. Reynolds stress $\langle u'v'\rangle/U^2$ is an indicator of the increased coupling and thereby the amplitude of the gravity standing wave oscillation. Enhanced $\langle u'v'\rangle/U^2$ increases the entrainment demand of the separated shear layer along the opening of the cavity, and affects the mass exchange process between the cavity and the main stream. It is therefore possible to anticipate that mass exchange will be higher as the values of Reynolds stress increases. For the transverse mode, the peak magnitude of $\overline{E(t)}$ along the trailing (downstream) cavity is relatively larger than along the leading (upstream) cavity, due to the larger magnitude of the Reynolds stress concentration. The same general observation holds for the longitudinal mode of the gravity standing wave, although the peak value of $\overline{E(t)}$ is only marginally larger for the trailing cavity, relative to the leading cavity.

As stated previously, the value of exchange velocity $\overline{E(t)}$ is larger along both cavities for the transverse mode ($U/f_nL = 2.9$). Thus, one can anticipate an increase of the dimensionless mass exchange coefficient for the transverse mode of the gravity standing wave. The values of mass exchange coefficient $k = \overline{E(t)}/2U$ are respectively, in presence of longitudinal and transverse modes of the gravity standing wave, $k = 0.032$ and 0.048 for the leading cavity, and $k = 0.035$ and 0.061 for the trailing cavity. The presence of the transverse gravity standing wave therefore results in an increase of the mass exchange coefficient k in the range of 50–74 %, relative to the longitudinal gravity standing wave.

https://doi.org/10.1017/jfm.2014.548 Published online by Cambridge University Press

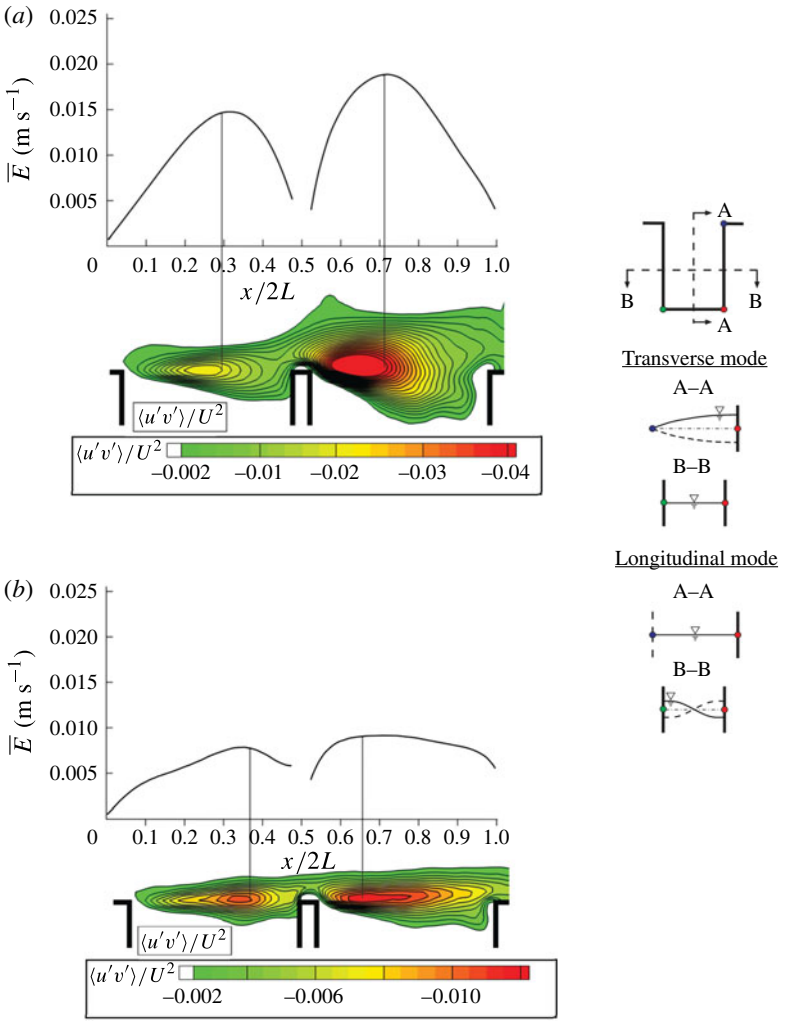


FIGURE 14. (Colour online) Patterns of time-averaged entrainment velocity ($\overline{E(t)}$) and Reynolds stress ($\langle u'v'\rangle/U^2$) along mouth ($y=0$) of cavities, for transverse and longitudinal modes of gravity standing waves within cavities, are represented respectively by images in (*a*) and (*b*).

8. Conclusions

Flow past a single cavity is well known to give rise to pronounced self-excited oscillations, due to resonant coupling between the unstable shear layer along the cavity opening and a standing wave mode within the cavity. In contrast, the occurrence of such oscillations due to flow past successive cavities has remained unclarified. The present investigation indicates that highly coherent oscillations of the flow structure can indeed be generated, even from a nominally turbulent state. The physics has been pursued with a technique of high-image-density PIV in conjunction with unsteady pressure measurements.

Onset of these highly coherent oscillations involves occurrence of a resonant peak of the unsteady pressure amplitude within the cavity when the reduced velocity is varied.

https://doi.org/10.1017/jfm.2014.548 Published online by Cambridge University Press

This resonant state occurs simultaneously in each of the successive cavities, thereby indicating a globally coupled resonant response.

The criteria for attainment of this resonant state, that is the occurrence of self-sustained oscillations, are twofold. First of all, a defined phase shift between the standing wave oscillations within successive cavities must be satisfied. This phase shift can take on values of either $\pi/2$ or π, depending on the orientation of the standing wave mode, that is, transverse or longitudinal. Second, an overall phase shift criteria must be satisfied in the separated shear layer along the openings of the cavities; in other words, the transverse undulations of the separated layer exhibit a phase difference of either π or 2π between the separation corner and the impingement corner of a given cavity, depending upon the orientation of the gravity standing wave in each cavity. Taken together, these two types of phase shifts allow maintenance of the self-sustained oscillation.

The time- and phase-averaged representations of the flow structure along and within the successive cavities are interpreted in terms of vorticity, velocity and streamline topology. The timing of vortex formation and impingement along the successive cavities are characterized in terms of patterns of phase-referenced vorticity, which shows analogous, but phase-shifted, clusters of vorticity along successive cavities. These patterns of time-dependent vorticity are compatible with regions of outflow and inflow that extend continuously from deep within the cavity across the separated shear layer. That is, compatibility exists between the dynamics of the recirculation zone within the cavity and the separated shear layer along the cavity opening. Patterns of streamline topology indicate that, if the oscillation amplitude is sufficiently large, mass transfer occurs between successive cavities during a portion of the oscillation cycle; such transfer is, however, not a necessary condition for the occurrence of a locked-on state of the system of successive cavities.

A consequence of these locked-on states of the highly coherent oscillations of the flow in successive cavities is generation of concentrated regions of Reynolds stress, which, in turn, are related to the magnitudes of the mass exchange between the cavity and the mainstream. The magnitudes of both the Reynolds stress and the mass exchange are a strong function of the orientation of the gravity standing wave, i.e. transverse versus longitudinal, in successive cavities.

Acknowledgement

The support of the National Science Foundation, grant CBET-0965293, is gratefully acknowledged.

REFERENCES

ADRIAN, R. J. & WESTERWEEL, J. 2010 *Particle Image Velocimetry*. Cambridge University Press.

ALAVIAN, V. & CHU, V. H. 1985 Turbulent exchange flow in shallow compound channel. In *Proceedings of the 21st International Congress of IAHR*, pp. 446–451.

BABARUTSI, S. & CHU, V. H. 1991 Dye-concentration distribution in shallow recirculating flows. *J. Hydraul. Engng* **117**, 643–659.

BABARUTSI, S. & CHU, V. H. 1993 *Reynolds-stress model for quasi-two-dimensional turbulent shear flow*, Engineering Turbulence Modelling and Experiments, vol. 2, pp. 93–102. Elsevier.

BABARUTSI, S. & CHU, V. H. 1998 Modeling transverse mixing layer in shallow open-channel flows. *J. Hydraul. Engng* **124**, 718–727.

BABARUTSI, S., GANOULIS, J. & CHU, V. H. 1989 Experimental investigation of shallow recirculating flows. *J. Hydraul. Engng* **115**, 906–924.

https://doi.org/10.1017/jfm.2014.548 Published online by Cambridge University Press

BASLEY, J., PASTUR, L. R., LUSSEYRAN, F., FAURE, T. M. & DELPRAT, N. 2011 Experimental investigation of global structures in an incompressible cavity flow using time-resolved PIV. *Exp. Fluids* **50** (4), 905–918.

BIAN, S., DRISCOLL, J. F., ELBING, B. R. & GECCIO, S. L. 2011 Time resolved flow-field measurements of a turbulent mixing layer over a rectangular cavity. *Exp. Fluids* **51**, 51–63.

BIRON, P. M., RAMAMURTHY, A. S. & HAN, S. 2004 Three-dimensional numerical modeling of mixing at river confluences. *J. Hydraul. Engng* **130**, 243–253.

BOOIJ, R. & TUKKER, J. 2001 Integral model of shallow mixing layers. *J. Hydraul Res.* **39**, 169–179.

CHU, V. H. & BABARUTSI, S. 1988 Confinement and bed-friction effects in shallow turbulent mixing layers. *J. Hydraul. Engng* **114**, 1257–1274.

CHU, V. H., WU, J. H. & KHAYAT, R. E. 1991 Stability of transverse shear flows in shallow open channels. *J. Hydraul. Engng* **117**, 1370–1388.

CONSTANTINESCU, G., SUKHODOLOV, A. & MCCOY, A. 2009 Mass exchange in a shallow channel flow with a series of groynes: LES study and comparison with laboratory and field experiments. *Environ. Fluid Mech.* **9**, 587–615.

EKMEKCI, A. & ROCKWELL, D. 2007 Oscillation of shallow flow past a cavity: resonant coupling with a gravity wave. *J. Fluids Struct.* **23** (6), 809–838.

EKMEKCI, A. & ROCKWELL, D. 2010 Effects of a geometrical surface disturbance on flow past a circular cylinder: a large-scale spanwise wire. *J. Fluid Mech.* **665**, 120–157.

ENGELHARDT, C., KRUGER, A., SUKHODOLOV, A. & NICKLISCH, A. 2004 A study of phytoplankton spatial distributions, flow structure and characteristics of mixing in a river reach with groynes. *J. Plankton Res.* **26**, 1351–1366.

ERCAN, A. & YOUNIS, B. A. 2009 Prediction of bank erosion in a reach of the sacramento river and its mitigation with groynes. *Water Resour. Manage.* **23**, 3121–3147.

FIEDLER, H. E. & MENSING, P. 1985 The plane turbulent shear layer with periodic excitation. *J. Fluid Mech.* **150** (1), 281–309.

FUJIHARA, M., SAKURAI, Y. & OKAMOTO, T. 2011 Hydraulic structure and material transport in an irrigation channel with a side-cavity for aquatic habitat. *Trans. Japan. Soc. Irrig. Drain. Rural Engng* **78**, 17–22.

GHIDAOUI, M. S. & KOLYSHKIN, A. A. 1999 Linear stability analysis of lateral motions in compound open channels. *J. Hydraul. Engng* **125**, 871–880.

IKEDA, S., YOSHIKE, T. & SUGIMOTO, T. 1999 Experimental study on the structure of open channel flow with impermeable spur dikes. *Annu. J. Hydraul. Engng-JSCE* **43**, 281–286.

JIRKA, G. H. 2001 Large scale flow structures and mixing processes in shallow flows. *J. Hydraul. Res.* **39**, 567–573.

JIRKA, G. H. & UIJTTEWAAL, W. S. J. 2004 *Shallow Flows: a Definition*. Taylor and Francis.

KADOTANI, K., FUJITA, I., MATSUBARA, T. & TSUBAKI, R. 2008 Analysis of water surface oscillation at open channel side cavity by image analysis and large eddy simulation. In *ICHE Conference*.

KANG, J., YEO, H. & KIM, C. 2012 An experimental study on a characteristics of flow around groyne area by install conditions. *Engineering* **4**, 636–645.

KIMURA, I. & HOSODA, T. 1997 Fundamental properties of flows in open channels with dead zone. *J. Hydraul. Engng* **123**, 98–107.

KNISELY, C. & ROCKWELL, D. 1982 Self-sustained low-frequency components in an impinging shear layer. *J. Fluid Mech.* **116**, 157–186.

KOLYSHKIN, A. A. & GHIDAOUI, M. S. 2002 Gravitational and shear instabilities in compound and composite channels. *J. Hydraul. Engng* **128**, 1076–1086.

KOLYSHKIN, A. A. & GHIDAOUI, M. S. 2003 Stability analysis of shallow wake flows. *J. Fluid Mech.* **494**, 355–377.

KURZKE, M., WEITBRECHT, V. & JIRKA, G. H. 2002 Laboratory concentration measurements for determination of mass exchange between groin fields and main stream. In *Proceedings of the IAHR Congress*.

https://doi.org/10.1017/jfm.2014.548 Published online by Cambridge University Press

LIU, X. & KATZ, J. 2011 Time resolved PIV measurements elucidate the feedback mechanism that causes low-frequency undulation in an open cavity shear layer. In *9th International Symposium on Particle Image Velocimetry-PIV11*, pp. 21–23.

MCCOY, A., CONSTANTINESCU, G. & WEBER, L. 2007 A numerical investigation of coherent structures and mass exchange processes in channel flow with two lateral submerged groynes. *Water Resour. Res.* **43**, W05445.

MCCOY, A., CONSTANTINESCU, G. & WEBER, L. 2008 Numerical investigation of flow hydrodynamics in a channel with a series of groynes. *J. Hydraul. Engng* **134**, 157–172.

MICHALKE, A. 1964 On the inviscid instability of the hyperbolictangent velocity profile. *J. Fluid Mech.* **19** (04), 543–556.

MICHALKE, A. 1965 On spatially growing disturbances in an inviscid shear layer. *J. Fluid Mech.* **23** (3), 521–544.

MIZUMURA, K. & YAMASAKA, M. 2002 Flow in open-channel embayments. *J. Hydraul. Engng* **128**, 1098–1101.

MUTO, Y., IMAMOTO, H. & ISHIGAKI, T. 2000 Turbulence characteristics of a shear flow in an embayment attached to a straight open channel. In *Proceedings of the 4th International Conference on HydroScience and Engineering*, p. 232. IAHR.

NAUDASCHER, E. & ROCKWELL, D. 1994 *Flow-Induced Vibrations: an Engineering Guide*. Dover Publications, Inc.

NAZAROVS, S. 2005 Stability analysis of shallow wake flows with free surface. In *Proceedings of the International Conference on Theory and Application of Mathematics and Informatics*, pp. 345–354.

NEZU, I. & ONITSUKA, K. 2002 PIV measurements of side-cavity open-channel flows-wando model in rivers. *J. Vis.* **5**, 77–84.

OHMOTO, T., HIRAKAWA, R. & WATANABE, K. 2005 Flow patterns and exchange processes in dead zones of rivers. In *31st IAHR Congress*, pp. 347–348.

OHMOTO, T., HIRAKAWA, R. & WATANABE, K. 2009 Effects of spur dike directions on river bed forms and flow structures. In *Advances in Water Resources and Hydraulic Engineering*, pp. 957–962. Springer.

RIBI, J. M., BOILLAT, J. L. & SCHLEISS, A. J. 2010 Flow exchange between a channel and a rectangular embayment equipped with a diverting structure. In *Proceedings International Conference on Fluvial Hydraulics*, pp. 665–671. IAHR.

RIVIERE, N., GARCIA, M., MIGNOT, E. & TRAVIN, G. 2010 Characteristics of the recirculation cell pattern in a lateral cavity. In *Proceedings International Conference on Fluvial Hydraulics*, pp. 673–679. IAHR.

ROCKWELL, D. 1983 Oscillations of impinging shear layers. *AIAA J.* **21**, 645–664.

ROCKWELL, D. & NAUDASCHER, E. 1978 Review: self-sustaining oscillations of flow past cavities. *Trans. ASME J. Fluids Engng* **100** (2), 152–165.

ROCKWELL, D. & NAUDASCHER, E. 1979 Self-sustained oscillations of impinging free shear layers. *Annu. Rev. Fluid Mech.* **11**, 67–94.

SANJOU, M. & NEZU, I. 2013 Hydrodynamic characteristics and related mass-transfer properties in open-channel flows with rectangular embayment zone. *Environ. Fluid Mech.* **13**, 527–555.

SHANKAR, P. N. & DESHPANDE, M. D. 2000 Fluid mechanics in the driven cavity. *Annu. Rev. Fluid Mech.* **32** (1), 93–136.

SOCOLOFSKY, S. A. & JIRKA, G. H. 2004 Large-scale flow structures and stability in shallow flows. *J. Environ. Engng Sci.* **3**, 451–462.

STANSBY, P. K. 2003 A mixing-length model for shallow turbulent wakes. *J. Fluid Mech.* **495**, 369–384.

SUKHODOLOV, A., ENGELHARDT, C., KRUGER, A. & BUNGARTZ, H. 2004 Case study: turbulent flow and sediment distributions in a groyne field. *J. Hydraul. Engng* **130**, 1–9.

SUKHODOLOV, A., UIJTTEWAAL, W. S. J. & ENGELHARDT, C. 2002 On the correspondence between morphological and hydrodynamical patterns of groyne fields. *Earth Surf. Process. Landf.* **27**, 289–305.

https://doi.org/10.1017/jfm.2014.548 Published online by Cambridge University Press

TANG, Y. P. & ROCKWELL, D. 1983 Instantaneous pressure fields at a corner associated with vortex impingement. *J. Fluid Mech.* **126**, 187–204.

TUKKER, J. & BOOIJ, R. 1996 The influence of shallowness on large-scale coherent structures. In *Advances in Turbulence VI*, pp. 141–144. Springer.

TUNA, B. A., TINAR, E. & ROCKWELL, D. 2013 Shallow flow past a cavity: globally coupled oscillations as a function of depth. *Exp. Fluids* **54**, 1–20.

UIJTTEWAAL, W. S. J. 2005 Effects of groyne layout on the flow in groyne fields: laboratory experiments. *J. Hydraul. Engng* **131**, 782–791.

UIJTTEWAAL, W. S. J. 2011 Horizontal mixing in shallow flows. In *34th IAHR World Congress*, pp. 3808–3814.

UIJTTEWAAL, W. S. J. & BOOIJ, R. 2000 Effects of shallowness on the development of free-surface mixing layers. *Phys. Fluids* **12**, 392–402.

UIJTTEWAAL, W. S. J., LEHMANN, D. & MAZIJK, A. V. 2001 Exchange processes between a river and its groyne fields: model experiments. *J. Hydraul. Engng* **127**, 928–936.

UIJTTEWAAL, W. S. J. & TUKKER, J. 1998 Development of quasi two-dimensional structures in a shallow free-surface mixing layer. *Exp. Fluids* **24**, 192–200.

VAN PROOIJEN, B. C. & UIJTTEWAAL, W. S. J. 2002 A linear approach for the evolution of coherent structures in shallow mixing layers. *Phys. Fluids* **14**, 4105–4114.

WALLAST, I., UIJTTEWAAL, W. S. J. & VAN MAZIJK, A. 1999 Exchange processes between groyne field and main stream. In *Proceedings from the 28th IAHR Congress*.

WEITBRECHT, V. & JIRKA, G. H. 2001 Flow patterns and exchange processes in dead zones of rivers. In *Proceedings of the IAHR Congress*, pp. 439–445.

WOLFINGER, M., OZEN, C. A. & ROCKWELL, D. 2012 Shallow flow past a cavity: coupling with a standing gravity wave. *Phys. Fluids* **24**, 104103.

YAEGER, M. & DUAN, J. 2010 Mean flow and turbulence around two series of experimental dikes. In *World Environmental and Water Resources Congress*, pp. 1692–1701.

YOSSEF, M. F. & DE VRIEND, H. J. 2011 Flow details near river groynes: experimental investigation. *J. Hydraul. Engng* **137**, 504–516.

https://doi.org/10.1017/jfm.2014.548 Published online by Cambridge University Press